UCSF
UC San Francisco Previously Published Works

Title

A novel reticular node in the brainstem synchronizes neonatal mouse crying with breathing

Permalink

https://escholarship.org/uc/item/6nn929cd

Journal

Neuron, 110(4)

ISSN

0896-6273

Authors

Wei, Xin Paul
Collie, Matthew
Dempsey, Bowen
et al.

Publication Date

2022-02-01

DOI

10.1016/j.neuron.2021.12.014

Copyright Information

Peer reviewed

A novel reticular node in the brainstem synchronizes neonatal mouse crying with breathing

Xin Paul Wei[1,2], **Matthew Collie**[1,†], **Bowen Dempsey**[3], **Gilles Fortin**[3], **Kevin Yackle**[1,4,*]

[1]Department of Physiology, University of California-San Francisco, San Francisco, CA 94143, USA

[2]Biomedical Sciences Graduate Program, University of California-San Francisco, San Francisco, CA 94143, USA

[3]Institut de Biologie de l'École Normale Supérieure (IBENS), École Normale Supérieure, CNRS, INSERM, PSL Research University, Paris, France

[4]Lead contact

Summary:

Human speech can be divided into short, rhythmically-timed elements, similar to syllables within words. Even our cries and laughs, as well as the vocalizations of other species, are periodic. However, the cellular and molecular mechanisms underlying the tempo of mammalian vocalizations remain unknown. Furthermore, even the core cells that produce vocalizations remain ill-defined. Here we describe rhythmically-timed neonatal mouse vocalizations that occur within single breaths, and identify a brainstem node that is necessary for and sufficient to structure these cries, which we name the intermediate reticular oscillator (iRO). We show that the iRO acts autonomously and sends direct inputs to key muscles and the respiratory rhythm generator in order to coordinate neonatal vocalizations with breathing, as well as paces and patterns these cries. These results reveal that a novel mammalian brainstem oscillator embedded within the conserved breathing circuitry plays a central role in the production of neonatal vocalizations.

eTOC

Speech and innate vocalizations have stereotyped and rhythmic elements, like syllables, suggesting a hardwired motor program underlies their production. Here, Wei et al. identify a

---

vocalization central pattern generator, the first of its kind, that coordinates neonatal mouse cries with breathing and encodes the rhythmic syllable structure.

Introduction:

Rhythmicity underlies both human speech and animal vocalizations. For instance, speech oscillates in volume with each syllable (Poeppel and Assaneo, 2020), the communicative calls of marmosets are composed of repeating units (Pomberger et al., 2018), and the timing of songbird syllables are regularly spaced as they learn to sing (Okubo et al., 2015). These and other examples suggest that the tempo of sounds within vocalizations is innately encoded. Indeed, the rhythmic vocalizations of midshipman fish are timed by pacemaker neurons in the hindbrain (Chagnaud et al., 2011). It has therefore been hypothesized that the rhythmicity of mammalian sound production is created by hardwired neural circuits in the brainstem, but evidence to support this theory is lacking.

The innate vocalization motor program is initiated by brainstem projections from the midbrain periaqueductal gray (Tschida et al., 2019); however, the neural circuitry required to fully orchestrate these vocalizations remains poorly understood (Hage, 2009; Zhang and Ghazanfar, 2020). Moreover, because mammalian vocalizations are produced by the concerted activity of sound producing (laryngeal), articulating (tongue), and breathing (diaphragm and intercostal) muscles (Riede, 2018), they must be seamlessly integrated with the breathing rhythm. We hypothesized that the vocalization motor patterning system is anatomically and functionally connected to the neural circuit for breathing in the brainstem. We also predicted that this circuit encodes rhythmicity within vocalizations. Here, by studying the neural control of instinctive cries produced by neonatal mice, which are analogous to the cries of human infants (Ehret, 2005; Long and Hull, 1961; Wilder, 1974), we elucidate the brainstem mechanism that patterns and paces mammalian vocalizations.

We found that neonatal cries contain one, two, three or more regularly spaced syllables within a single breath. Our identification and characterization of the cry premotor node iRO, which produces a fast and autonomous rhythm nested within a slower breathing rhythm, provides a mechanism for this rhythmic cry production. Ablation or pharmacological inhibition of the iRO either eliminates or modifies normal neonatal cry rhythms and disrupts multisyllabic cries. Brief activation of the iRO neurons during an endogenous cry adds a syllable, while excitation during calm breathing initiates an ectopic cry bout.

Results:

Neonatal cries comprise syllables that are rhythmically timed within a breath.

To study the coordination of vocalizations with breathing, we induced innate ultrasonic vocalizations (USVs) by removing neonatal mice from their nests. Cries and breathing were recorded by unrestrained barometric plethysmography (Hernandez-Miranda et al., 2017). Cries had increased inspiratory and expiratory airflow coupled with USVs (50-150 kHz) and occurred in bouts of 9.7±0.6 breaths (avg. ± SEM, 16 pups) (Figures 1A–C). Most cry breaths comprised one distinct USV, or syllable, that commenced ~10-20 milliseconds after

expiration onset, coinciding with peak airflow (Figures 1D, F–G). However, cry breaths in the middle of a bout tended to include two, three, or sometimes more elements, and were therefore designated as multisyllabic (Figures 1C–D). In these cases, each syllable onset was timed to follow rhythmic local peaks in expiratory airflow that were separated by a period of silence and an airflow dip (Figures 1D, F–G). Unisyllabic cry syllables were longer than those in multisyllabic cries, and syllables progressively increased in length during multisyllabic cries (Figure 1E). The rhythmicity of cries led us to hypothesize that they were timed by a fast conditional oscillator nested within slower breathing.

Cry syllables are coordinated with the respiratory motor program.

Murine adult vocalizations are produced when airflow through a closed (adducted) glottis becomes rapid and then turbulent after colliding with the laryngeal cartilage (Johnson et al., 2010; Mahrt et al., 2016). To explore if neonatal cries similarly require laryngeal adduction, we disrupted the thyroarytenoid (TA) muscle, a key laryngeal adductor. Bilateral electrolytic TA lesion eliminated the characteristic spectrogram features of cries despite the retention of augmented airflow, rate, and regularity during cry bouts (Figures 2A, S1). Surprisingly, attempted cry breaths after TA lesion still showed airflow oscillations reminiscent of multisyllabic cries (Figure 2B). This suggested that, although laryngeal adduction is required for producing the sound of each cry syllable, the airflow dip that separates the syllables is generated by a distinct mechanism.

Because the larynx adducts immediately after inspiration during basal breathing (Del Negro et al., 2018), we wondered if the airflow dips that preceded laryngeal adductions during cry syllables are also patterned by an inspiratory motor program. In this way, inspiration would be ectopically initiated during expiration. Indeed, signatures of the inspiratory motor program, such as genioglossus (tongue) and intercostal muscle activity (Huckstepp et al., 2016), preceded each cry syllable during airflow dips (Figures 2C–D). Muscle activity was maximal approximately halfway between two expiratory airflow peaks, during which time, body wall movements mimicked inspiration (Figures 2E, S2 and Video S1). These data suggest that the proposed oscillator can time multisyllable cries by cyclically re-engaging the respiratory motor program to generate inspiration followed by laryngeal adduction within a slower breath.

The medullary brainstem contains a cluster of premotor neurons for sound production and articulation.

To begin investigating the underlying circuit driving rhythmic cries, we sought to identify premotor neurons to the key muscles that produce sound, including the TA and cricothyroid (CT) muscles that adduct the larynx. We thus performed monosynaptic viral tracing from TA and CT motor neurons by restricted G-rabies injection into either muscle (Figure 3A, see methods). Four to seven days after injection, we found infected neurons arising from both muscles in similar areas throughout the ventral respiratory column (n=10 TA; n=10 CT) (Figure S3). Traced premotor neurons were distinguished from motor neurons by the absence of *Phox2b* transcription factor expression (Pattyn et al., 2000) and were found medial to the compact nucleus ambiguus (cNA) in the rostral ventral intermediate reticular formation (rv-iRF), the Bötzinger complex (BötC), the preBötzinger complex (preBötC),

and the retroambiguus (RAm) (Figures 3A–C, S3). To find the neurotransmitter used by these various TA premotor neuron pools, we repeated the rabies tracing in transgenic neonatal mice where glutamatergic or GABAergic neurons were labeled. TA premotor neurons within the rv-iRF were *Vglut2*⁺, those in other respiratory brainstem centers including the BötC and RAm were mostly *Vgat*⁺ and those in the preBötC were either *Vglut2*⁺ or *Vgat*⁺ (Figures 3C–D).

We next asked whether premotor neurons for muscles of articulation, such as the tongue, overlap with one or more laryngeal premotor neuron clusters. To directly compare their spatial distributions, we microinjected the tongue and TA with ΔG-rabies-expressing GFP or mCherry, respectively. Tongue premotor neurons primarily localized to the iRT (Figure 3E, see Stanek et al. 2014). Therefore, of the areas that contained TA premotor neurons, only the rv-iRF contained neurons premotor to the tongue (Figure 3E). Some neurons in this region even innervated both the TA and the tongue. Although the rv-iRF is distinct from brainstem sites that have previously been implicated in vocalization, such as the caudal RAm (Tschida et al., 2019), it is apparently unique in containing excitatory premotor neurons for multiple muscles of phonation. It therefore became the prime candidate for our proposed oscillator to pace and pattern neonatal cries.

The rv-iRF containing the premotor cluster is required for neonatal crying but not breathing.

We sought to test the necessity of the rv-iRF for patterning neonatal crying by measuring breathing and cries before and after bilateral electrolytic lesion of the phonatory premotor neuron cluster medial to the cNA. Each animal's cry and breath parameters were measured 24 hours after lesion and normalized to pre-lesion data. The anatomical location of the lesions (along with other criteria, see methods) allowed us to classify them as bilateral on-target, bilateral off-target, or unilateral on-target (n = 5, 7 and 6). Lesions were approximately 100-200μm in diameter and on-target lesions were limited to the region medial to the cNA (Figures 3, 4B).

Neonates with bilateral on-target lesions still attempted to vocalize (Figure 4E, on-target post : pre total bouts 0.86±0.14 vs. off- 1.08±0.19, p = 0.2, t-test) by augmenting inspiratory and expiratory airflows (expiratory- 0.89 ± 0.27 vs. 1.10 ± 0.07, p = 0.25 and inspiratory- 0.92 ± 0.30 vs. 1.13 ± 0.13, p = 0.27), showing that the rv-iRF is not the endogenous cry initiating signal. Instead, the breaths in each bout failed to produce normal cries (Figure 4E) and commonly exhibited irregular airflow (Figure 4A vs 4C). Bilateral on-target lesions resulted in fewer unisyllabic and multisyllabic cries compared to off-target (Figure 4F) and the few apparently normal augmented cry breaths were less likely to result in vocalizations (Figures 4A, E–F). Furthermore, the very scarce successful cries were abnormally short (Figure 4H). For each of these parameters, unilateral on-target lesions resulted in intermediate phenotypes (Figures 4E–H). Importantly, basal breathing frequency and regularity was unchanged in all lesioned animals (Figures 4G and S1). Moreover, impaired crying in neonates with on-target lesions is unlikely to be attributed to the ablation of TA or CT motor neurons, which reside more caudal (>400μm, Figures 3C and S3) and/or ventral to the area of on-target lesions (Hernández-Morato et al., 2013; Patrickson

et al., 1991), although we cannot definitively rule this out. Indeed, even off-target lesions that partially included the cNA resulted in normal crying. Together, these data demonstrate that the patterning of neonatal cry bouts and the cries within a breath requires the rv-iRF, which contains premotor neurons for multiple phonatory muscles (Figure 3), but that the augmentation of cry breaths and basal breathing are independent of this proposed oscillator.

The rv-iRF is sufficient to produce neonatal crying.

The necessity of the rv-iRF for correct production of the cry motor program indicates it plays either a 'central' or 'ancillary' role. We hypothesized that if selective activation of the rv-iRF induced ectopic crying, then it would implicate the rv-iRF as the core of the motor program. We micro-stimulated the neonatal rv-iRF unilaterally with very short pulses of low amplitude current that was incrementally increased while monitoring breathing and sound production (4x0.4ms biphasic pulses, 50μA and up to 600μA). Surprisingly, upon reaching a current threshold in most animals, the brief pulse reliably transformed basal breathing into an entire cry bout (Figure 5A, n=11/13 animals). The anatomical location of the electric stimulation was determined by the focal region of tissue damage and when low current amplitudes triggered cry bouts (150μA), the targeted area resided within or immediately nearby (<150μm) the rv-iRF (n=8). When significant current amplitudes were required to or failed to trigger a cry bout (>160-600μA), the stimulated area was rostral or caudal to the rv-iRF (n=5) (Figure 5C). The cry bouts after on-target stimulation started within ~200ms of the stimulus and were approximately normal in length (7.4±0.8 breaths vs. 9.7±0.6 breaths in baseline recordings) (Figure 5B). Since the cry bouts last for several seconds beyond the 10ms electrical pulse, a self-sustaining system within the rv-iRF is likely engaged. And most importantly, this result, combined with the loss-of-function lesions, shows that the rv-iRF is a 'central' component in patterning neonatal cry.

A novel oscillator in the rv-iRF is active during expiration.

We hypothesized that if the premotor cluster in the rv-iRF is the oscillator that controls fast rhythmic cries nested within a slower breathing pattern, its constituent neurons would oscillate faster than the preBötC inspiratory rhythm generator (Smith et al., 1991). We tested this idea using simultaneous recordings of rabies-traced TA premotor neurons in the rv-iRF and preBötC inspiratory activity in the hypoglossal nerve (cranial nerve XII) in medullary brainstem slices from neonatal mice. Whole cell recordings of premotor neurons revealed a rhythmic oscillation of membrane potential throughout expiration (every 6.2±1.6s), which was faster than the rhythm of preBötC bursts (separated by 23.1±1.8s, see methods for discussion of these rates) (Figures 6A, C). To determine if this activity extends throughout the rv-iRF or perhaps beyond, we monitored the electrophysiological activity of a premotor neuron while simultaneously imaging panneural GCaMP6s fluorescence emitted in slices from *Snap25*-GCaMP6s transgenic mice. Only neurons located in an area directly medial to the cNA displayed synchronized rhythmic changes in fluorescence during expiration, coincident with the TA premotor neuron activity (Figures 6A–B). The synchronicity of the rhythmic activity was validated by paired whole cell recordings (Figure 6D) and the rhythmic activity was even synchronized bilaterally (Figure 6E). This region precisely coincided with the rv-iRF and thus, we named this cluster of dozens of neurons the intermediate reticular oscillator (iRO).

Moreover, when fast synaptic communication between neurons was prevented with a cocktail of synaptic transmission blockers (NBQX, APV, picrotoxin, and strychnine), all the iRO neurons retained synchronous rhythmic oscillations in electrical activity and *Snap25*-GCaMP6s fluorescence (Figures 6F and S5). This uniquely defining feature further distinguished them from other nearby neurons and the preBötC. This iRO oscillatory activity was found in rabies-traced TA (Figure S5A), CT, and tongue premotor neurons (Figure S4A) in the area, but not premotor neurons for other orofacial oscillators (Figure S4B) or respiratory centers in the brainstem (Table S1). We thus concluded that the iRO is a novel oscillatory node within the medullary brainstem, and it is uniquely composed of premotor neurons for multiple muscles of vocalization.

We next investigated the mechanism underlying the oscillatory behavior of the iRO neurons. In the presence of synaptic blockers, each iRO neuron displayed a rhythmically-timed inward current when the membrane potential was clamped at −80 mV, which was eliminated by the gap junction antagonists carbenoxolone (cbx), 18ß-glycyrrhetinic acid, and meclofenamic acid (Figure S5F). Furthermore, the rhythmic activity in an iRO neuron persisted when voltage-gated sodium channels were blocked only within the patched neuron but was abolished when these sodium channels were blocked in nearby neurons (Figure S5D). And lastly, the iRO neurons showed direct electrical coupling (Figure S5E). These data affirm that iRO neurons are coupled by gap junctions and that this, rather than fast synaptic signaling, is required for the autonomous oscillatory behavior that is unique to the iRO.

Using depolarizing and hyperpolarizing neuromodulators, we revealed that the iRO rhythm ceased upon network hyperpolarization and was therefore voltage dependent (Figures S6A–B). This conditional rhythmic activity is consistent with the intermittent nature of crying. The canonical I_h pacemaker current (Kaupp and Seifert, 2001) was not involved in setting the interburst interval (antagonist, ZD7288). However, block of the depolarizing persistent sodium current I_{NaP} eliminated the rhythm (riluzole, Figure S6E), consistent with a role in setting the interburst interval, burst, or both (French et al., 1990; Yamanishi et al., 2018). Bursting was attenuated or prolonged by blocking or augmenting L-type calcium channel (LTCC) activity, respectively (nifedipine and bay K8644, Figures S6C–D), but was not affected by a T-type calcium channel antagonist (mibefradil). Surprisingly, burst termination was not affected by any of the calcium-activated potassium channel antagonists that we tested (IbTX, UCL 1684), but was altered by preventing voltage-gated sodium channel inactivation (veratridine, Figure S6F).

While iRO can oscillate independently from the preBötC (Figure 6F), the pharmacological profile provided an opportunity to determine if antagonizing the iRO rhythm impacted the preBötC. *In vitro*, bath application of the gap-junction (cbx) or LTCC (nifedipine) blockers did not change the preBötC rhythm, thereby demonstrating these two oscillators are distinct (Figures 6G–H). Next, to determine the requirement of the iRO rhythm for patterning neonatal cries, we measured breathing and vocalizations before and after bilaterally injecting the iRO with either cbx or nifedipine. Injection of cbx or nifedipine did not change the number or length of cry bouts but decreased the number of breaths with vocalizations in a cry bout and unisyllabic cry length, and appeared to only somewhat reduce the

proportion of cries with multiple syllables due to large variance in this parameter (Figures S7A–C). In contrast, injection of ACSF as a control only minimally impacted cries (Figures S7A–C). Consistent with our *in vitro* studies, basal breathing was unchanged by cbx or nifedipine (Figures S7C and S1). The changes observed in cries after pharmacologically antagonizing the iRO rhythm appear similar to those produced by electrolytic lesions, and thus demonstrated that the iRO's intrinsic rhythm is likely required for patterning neonatal cries within the breath, consistent with it being the proposed cry oscillator.

The iRO recruits the preBötC and laryngeal motor neurons to produce the cry motor program.

The first feature of the cry motor program is activation of inspiratory muscles that precedes the onset of each syllable (Figure 2). We postulated that the iRO triggers the inspiratory motor program via the preBötC. *In vitro*, ~50% of recorded preBötC neurons displayed excitatory postsynaptic potentials (EPSPs) coincident with each iRO oscillation and these disappeared after antagonizing the iRO rhythm with cbx (Figures 7B–C). This suggests an excitatory connection (direct or indirect) from the iRO to the preBötC. Furthermore, preBötC bursts occurred in phase with, or immediately after, the onset of iRO oscillations, showing that the iRO biases the timing of preBötC bursts (Figure 7C - consistent iRO oscillation preceding preBötC burst in PSTFI; and 7D –similar time intervals between iRO to iRO and iRO to preBötC bursts). Combined, these data demonstrate a physical and functional coupling of the iRO and preBötC rhythms. Thus, the iRO has the connectivity to initiate the inspiratory motor program that precedes each of the cry syllables within a breath. Note, although unlikely, we cannot eliminate a possible third center that simultaneously excites both the iRO and preBötC.

The second key feature of the cry motor program is the laryngeal adduction to produce sound that follows each inspiratory event, known as post-inspiratory activity (Riede, 2014) (Figure 2). In contrast to preBötC neurons, the excitation of iRO neurons during inspiration persisted through post-inspiration (Figure 7G). Because iRO neurons are glutamatergic and premotor to laryngeal adductors (Figures 3 and S3), their post-inspiratory activity is consistent with the ability to generate cries. However, an additional mechanism must be invoked to explain the prevention of laryngeal adduction during inspiration. We investigated this using voltage-clamp recordings of TA motor neurons *in vitro* following their identification by intramuscular injection of Alexa Fluor 555-conjugated cholera toxin B. Nearly all recorded TA motor neurons exhibited inhibitory synaptic currents during inspiration, and 60% displayed excitatory post-inspiratory activity, which we expected to result from the presynaptic iRO activity (Figure 7H). These excitatory and inhibitory inputs were also evident during each iRO oscillation (n = 12/22 motor neurons) (Figure 7H, red arrows). This *in vitro* activity mirrors the timing of laryngeal sound production during each cry syllable.

Blockade of excitatory synaptic transmission (CNQX and APV) silenced the preBötC (Smith et al., 1991) and even eliminated all inhibitory synaptic modulation of TA motor neurons (Figure 7I). As iRO remains rhythmic in this condition (Figures 6), the direct inhibitory input to TA motor neurons must therefore be from a different source, likely the

Vgat-positive TA premotor neurons within the preBötC or RAm (Figure 3). Upon blockade of inhibitory synaptic transmission (picrotoxin and strychnine), excitatory synaptic input remained and it accurately mimicked the iRO activity, as expected (Figure 7H vs. 7I). This connectivity between the iRO, the inhibitory inspiratory neurons, and TA motor neurons comprises a plausible mechanism by which the iRO patterns post-inspiratory laryngeal adduction and sound production. Thus, by recruiting the preBötC to drive the inspiratory motor program and directly activating laryngeal adductors post-inspiration, the iRO could pattern neonatal cries.

Optogenetic excitation of the iRO induced neonatal cry bouts and added an additional syllable.

The unique retention of synchronous rhythmic activity in synaptic blockers allowed us to screen fourteen Cre recombinase lines that might label the iRO (Cre > GCaMP6f, Table S1). We validated that the iRO is composed of only excitatory neurons and identified expression of two neuropeptides, *Penk* and *Tac1*. Co-expression of *Vglut2*-Flp and *Penk*-Cre labeled neurons within the iRO region (Figure 8A), and electrophysiological recordings of these neurons in synaptic blockers showed they were indeed the iRO (Figure 8B, n = 5/7 neurons). We could robustly depolarize the iRO neurons with light after expression of the ReaChR opsin with *Vglut2*-Flp and *Penk*-Cre (Figure 8B). Quantification of ReaChR^{+} neurons throughout the ventrolateral medulla showed numerous neurons within the iRO and some labeling within the Post-inspiratory Complex (only 23% of *ChAT*^{+} cells), the BötC, preBötC, and RAm (Figure 8C). The ability of ReaChR to depolarize the iRO, coupled with its expression pattern and careful fiber optic placement, offered the ability to ectopically activate the iRO *in vivo* during basal breathing and ongoing cries.

Triple transgenic neonates were unilaterally implanted with an optic fiber above or adjacent to the iRO and we ectopically activated the iRO with 1 to 2 seconds of 10Hz light during basal breathing. In most instances, several breaths were augmented, appearing similar to cry breaths (Figure 8D, 9/9 ReaChR[+]). Remarkably, in many cases basal breathing was transformed into a complete cry bout that persisted beyond the light pulse (Figure 8E, 5/9 ReaChR[+]), mirroring the effect of the rv-iRF electrical stimulation (Figure 5). The cry bouts started 2.1±0.9 seconds after the laser onset (0.6±0.9 seconds after laser offset) and appeared similar to endogenous cry bouts in length, 10.6±0.7 breaths versus 9.7±0.6 (Figure 8F). Cry bouts never occurred in wildtype controls after light pulses (Figure 8F, n=5). Since optogenetic activation of the iRO mimics the effect of localized electric stimulation of the rv-iRF, it is unlikely that the induced cry bouts result from activation of ReaChR^{+} neurons in other areas (like RAm). The sufficiency of the iRO to drive an ectopic cry bout is consistent with it playing a central role in patterning neonatal cries.

Next, we hypothesized that stimulation of the iRO with a triggered, single 50ms light pulse during or immediately after the first cry syllable would induce a second syllable (Figure 8G). This is indeed the case. Quantification of cry syllables (USV or the expiratory airflow peak that accompanies a syllable) showed an enrichment of bisyllabic cry breaths with light stimulation compared to a similarly triggered sham stimulation (Figure 8G, ratio of light : sham = 1.7±0.17, 9 ReaChR[+]). No difference was observed in control animals (light: sham

= 0.97±0.04, 6 animals) (Figure 8G) and basal breathing was unchanged by the 50ms light pulse (Figures 8H and S8). In summary, these optogenetic data demonstrate that activation of the iRO is sufficient to pattern the cry syllables within a breath and even sufficient to pattern entire cry bouts.

Discussion:

We have identified a novel brainstem node, the iRO, which acts as an autonomous oscillator that organizes the patterning of neonatal mouse vocalizations with breathing. Its proximity to the cNA is consistent with a previous hypothesis that a central pattern generator for vocalization resides in the medullary reticular formation (Hage, 2009). A simple model predicts that patterning of laryngeal and breathing motor groups is sufficient to control vocalizations (Zhang and Ghazanfar, 2020). Furthermore, it is anticipated that such a patterning system would also encode the tempo of syllables within vocalizations. Our results are consistent with such a model.

The iRO produces a conditional and flexible rhythm to time syllables.

The iRO rhythm requires gap junctions but not synaptic neurotransmission (Figure 6). Additionally, the speed of the rhythm can be tuned by membrane potential of the iRO network (Figure S6). In this way, electrical coupling integrates the membrane properties of all the iRO neurons, some of which may be intrinsic pacemakers, resulting in a robust, voltage-dependent, and tunable rhythm. Such a rhythm is to be expected for neonatal cries since they come-and-go in bouts, and the number of syllables within a cry breath is flexible, necessitating a conditional and tunable oscillator. In this model, the iRO would be most depolarized and oscillating fastest mid-bout, consistent with when we observe the most multisyllabic cries. Interestingly, momentary stimulation of the iRO triggered a prolonged cry bout (Figures 5 and 8), suggesting it may be a dynamical and self-sustaining system. Note, the different speeds of the iRO *in vitro* and syllables *in vivo* is likely due to less excitable conditions *in vitro* (like temperature and solutions) and removal of excitatory inputs in the slice. We refer to the iRO as an oscillator due to its autonomous *in vitro* rhythm and we hypothesize that it also oscillates *in vivo* during cries. A key future study will be to measure the iRO's activity during neonatal cries and validate that its intrinsic rhythm is required to pattern multisyllabic cries.

It will also be important to determine whether the iRO's role in timing syllable onset is generalizable to adult mouse vocalizations, as well as those of different species, and how this is utilized or bypassed during learned vocalizations or song. It is possible that more complex and diverse syllables, like that in human speech, result from learned fine motor control of the articulator muscles, but the rhythmic timing of sounds production remains patterned by innate iRO oscillations. Our identification of a molecular signature of iRO neurons ($Vglut2^+Penk^+$) will provide one avenue for these further investigations.

The iRO patterns the motor sequence to produce multisyllabic cries.

To our surprise, the motor pattern of multisyllabic neonatal cries is the fast recycling of the normal breath sequence – inspiratory activity followed by post-inspiratory laryngeal

adduction (Figure 2). In our model, iRO re-activates the preBötC, and thus inspiratory muscles, during the expiration of a cry breath. The opposing inspiratory force causes a dip in airflow that forms the gap between syllables. Each "inspiratory" dip is then followed by the natural post-inspiratory laryngeal adduction to produce sound. *In vitro*, the iRO has the connectivity to produce this entire motor sequence (Figure 7).

A commonly held notion is that vocalizations are simply produced by augmented expiratory airflow. In this model, the generation of a multisyllabic cry would involve an oscillator that drives multiple forced expirations within a breath, and the gaps between syllables would simply be brief pauses in expiration. However, this is not the case. To our knowledge, this study is the first time that that inspiration has been shown to be ectopically re-activated during expiration leading to a nested cry rhythm within breathing, implicating it as a key component of the vocalization motor program.

iRO fulfills the criteria to be a central pattern generator used in vocalization.

Central pattern generators (CPGs) are critical for making rhythmic and stereotyped motor sequences like walking. To be classified a CPG, a collection of neurons must autonomously produce a rhythm and also encode a motor pattern (Grillner and El Marina, 2020, Marder and Bucher, 2001). The iRO's intrinsic rhythm throughout expiration, its synaptic bilateral synchronization, the connectivity to coordinate inspiratory and laryngeal muscle activity, the necessity of it and its rhythm for neonatal cries, and its sufficiency to produce complete cry bouts and cry syllables fulfill the key criteria to define the iRO as a CPG used in vocalization. Importantly, lesion of the iRO impacts the motor pattern of cries, but not the number of attempted cry bouts, and stimulation during a cry can produce an extra syllable, demonstrating it is not simply an upstream cry initiation signal. And surprisingly, unlike other well characterized CPGs, the same iRO neurons participate in both pacing and patterning.

The midbrain periaqueductal gray (PAG) and the medullary nucleus tractus solitarius (NTS) are two additional brainstem sites implicated in vocalization (Tschida et al., 2019 and Hernandez-Miranda et al., 2017). Each region projects to expiratory and laryngeal motor neurons in the medullary RAm and are required for murine USVs. Here, we propose that the iRO is downstream of both and serves to pattern the breaths in a cry bout and the vocalizations within each breath. Also, we predict that the PAG and NTS inputs to RAm serve to augment airflow during the cry since the iRO lesions primarily alter the cry breath structure (Figure 4).

Our chosen *in vivo* approaches were influenced by the technical limitations of neonatal studies (e.g., absent AAV gene expression in several days), thus, although each experiment has caveats (e.g., electrolytic lesions of passing fibers or optogenetic excitation of nearby Vglut2+Penk+ neurons), the diversity of experiments with a unified impact upon cries has led us to the parsimonious model that the iRO patterns neonatal cries. Note, the observed latency to a cry bout after electrical or optogenetic stimulation may be due to the necessary recruitment of other cry associated areas (e.g., preBötC, RAm, NTS), but nonetheless, this does not preclude the iRO from being a crying CPG.

Is the iRO a component of the nearby respiratory centers?

Although the iRO is anatomically nearby or overlapping with the breathing control circuit (Del Negro et al., 2018), we believe it to be distinct. For example, although the iRO displays preBötC inspiratory activity, the iRO nor its intrinsic rhythm are required for the preBötC to pace inspiration (Figures 4, 6). Compared to the reported Post-inspiratory Complex (PiCo) (Anderson et al., 2016), the iRO does not possess the defining molecular or electrophysiological properties (e.g., *ChAT*-Cre but not *Dbx1*-Cre lineage, restricted postinspiratory activity, norepinephrine- and synapse-dependent rhythm). Importantly, the iRO is not required for the basal breathing pattern (Figures 4, S1) nor does momentary activation of the iRO shift the phase of a basal breath (Figures 8, S8, expected forward phase shift for preBötC or backward for PiCo). However, more studies are needed to definitively claim the iRO is completely distinct from these or other parts of the breathing control circuit. Other studies should aim to understand the interactions of these centers, such as if the preBötC re-times the iRO or if PiCo contributes to the iRO post-inspiratory activity. The medullary brainstem is packed with separate but interacting patterning systems that control behaviors like whisking, swallowing, and breathing (Del Negro et al., 2018), and we now add crying/vocalization to this list.

Disruptions to the iRO may have clinical implications.

Hardwired patterning systems like the iRO allow the brain to generate robust, reproducible motor tasks that are essential for innate behaviors, such as crying. Improper development or execution of the motor sequence encoded by the iRO may lead to significant communication deficits. Indeed, we show that neonatal mice with disrupted iRO activity fail to properly pattern vocalizations (Figure 4). Thus, this study opens a new possibility that patients with motor speech disorders, particularly those affected by mutism or oromotor dyspraxia, may have defects in the iRO or neural circuits connected to the iRO.

Might iRO be re-purposed for other behaviors?

Because the iRO can coordinate breathing with laryngeal adduction, we imagine that it may be repurposed for non-vocalization behaviors that also require laryngeal closure, including spontaneous laughter (Luschei et al., 2006; Titze et al., 2008) and swallowing (Jean, 2001; Prescott et al., 2020; Toor et al., 2019). Indeed, neurons within the anatomical region of the iRO have previously been implicated in swallowing (Toor et al., 2019). Both its restricted anatomical location and rhythmic activity make the iRO an ideal system for studying the role of higher brain centers and neuromodulation in sculpting or repurposing a pattern generating system to support a range of both innate and learned mammalian behaviors.

STAR Methods:

Resource Availability

Lead contact—Further information and requests for resources and reagents should be directed to and will be fulfilled by Kevin Yackle (kevin.yackle@ucsf.edu).

Materials availability—This study did not generate new unique reagents.

Data and code availability

- All reported data collected in this study will be shared by the lead author upon request.

- All original code has been deposited at Zenodo and is publicly available as of the date of publication. DOIs are listed in the key resources table.

- Any additional information required to reanalyze the data reported in this paper is available from the lead contact upon request.

Experimental model and subject details

C57Bl/6J, *Snap25-GCaMP6s* (*Snap25^{tm3.1Hze}*) (Madisen et al., 2015), *Slc17a6*-Cre (Vong et al., 2011), *Gad2*-Cre (Taniguchi et al., 2011), *Slc32a1*-Cre (Vong et al., 2011), *Slc6a5*-Cre (Sherman et al., 2015), *RIKEN-Slc6a5*-Cre (Kakizaki et al., 2017), *Dbx1*-Cre (Bielle et al., 2005), *Foxp2*-Cre (Rousso et al., 2016), *Chat*-Cre (Rossi et al., 2011), *Egr2*-Cre (Voiculescu et al., 2000), *Neurod6*-Cre (Schwab et al., 2000), *Penk*-Cre (Tasic et al., 2018), *Parv*-Cre (Hippenmeyer et al., 2005), *Tac1*-Cre (Harris et al., 2014), *Npy*-Cre (Milstein et al., 2015), ROSA-LSL-G-TVA (Gt(ROSA)26Sor^{tm1(CAG-RABVgp4,-TVA)Arenk}) (Takatoh et al., 2013), ROSA-LSL-GCaMP6s (Ai96) (Madisen et al., 2015), ROSA-LSL-GCaMP6f (Ai95) (Madisen et al., 2015), ROSA-LSL-EYFP (Srinivas et al., 2001), *Slc17a6*-FlpO (Daigle et al., 2018), RC::FLTG (Plummer et al., 2015), and R26-LSL-FSF-ReaChR-mCitrine (Hooks et al., 2015) have been described. Mice were housed in a 12-hour light/dark cycle with unrestricted food and water. Both male and female neonates were used in this study and the gender was not determined prior to the experiments performed. No sex specific effects on neonatal crying nor breathing were observed. All animal experiments were performed in accordance with national and Institutional Animal Care and Use Committee - University of California San Francisco guidelines with standard precautions to minimize animal stress and the number of animals used in each experiment.

Recombinant viruses—All viral procedures followed the Biosafety Guidelines approved by the University of California, San Francisco (UCSF) Institutional Animal Care and Use Program (IACUC) and Institutional Biosafety Committee (IBC). The following viruses were used: oG SiR G-Deleted Rabies-FlpO-mCherry, G-Deleted Rabies-eGFP, G-Deleted Rabies-mCherry (all $>1.0 \times 10^8$ TU/mL, The Viral Vector Core at the Salk Institute for Biological Sciences or Janelia Viral Tools) and HSV-hEF1a-Rabies G (RN700), HSV-hCMV-YTB (Gene Delivery Technology Core Massachusetts General Hospital).

Methods details

Plethysmography, vocalization, and analysis—Breathing pressure changes and vocalizations were measured in neonatal mice (P2-P4) in a custom prepared whole animal plethysmography chamber at room temperature (23°C, Figure 1a) and constant humidity. The top of the chamber is sealed by the microphone and enables the volume of the chamber to be appropriately adjusted to the size of the neonate. Pups were removed from their home cage and placed in the recording chamber for 2 x 5 minutes of recording and returned to their home cage. Mice were recorded for 1-2 more times throughout day, following the same protocol, to get a consistent baseline. Vocalization was recorded using

an Avisoft Bioacoustics UltraSoundGate CM16/CMPA microphone and chamber pressure was transmitted to a spirometer (AD Instruments). The microphone and spirometer were connected to a PCI DAQ device (PCI NIDAQ 6251), allowing respiration and vocalization data to be simultaneously acquired at 400kHz using custom Matlab (MathWorks) code. Light tapping of the chamber with a metal rod show a constant <2ms difference in timing of changes in sound and pressure change.

The respiration and vocalization data were analyzed offline in Matlab. The pressure trace was downsampled, filtered, and breathing was segmented using the troughs and peaks of measured pressure as surrogates for onset of inspiration and expiration, along with quality control metrics. Pressure change was defined as the first derivative of the pressure trace with respect to time. Given differences in tidal volume due to the intrinsic variance of lung volumes of pups at these ages (discussed further below), large breaths were defined as the minimal tidal volume that must be exceeded for 95% of cries in a trace. USVs were detected using code modified from the Holy Lab (Holy and Guo, 2005). The parameters used to detect vocalizations are: spectral purity threshold > 0.3, spectral discontinuity threshold < 0.8., cry duration threshold > 2ms, minimal inter-syllable interval > 15ms, and mean frequency threshold > 30kHz. Airflow peaks were determined using the findpeaks function (Matlab).

Since barometric whole-body plethysmography imprecisely measures airflow and tidal volume (Mortola and Frappell, 1998), tidal volume in neonates correlates with their weight instead of age (Lim et al., 2014), we have reported the breathing measurements as changes in pressure that are in arbitrary units. Thus, we have not compared the amplitude of breathing airflow between animals nor reported it as mLs/sec. However, these measurements still allow for the changes in breathing within the same animal to be directly compared as arbitrary units.

Genioglossus and intercostal EMG—Neonatal mice were briefly anaesthetized by hypothermia. Paired EMG electrodes made from Teflon-coated multistranded stainless steel wires (Cooner Wire) and small suture needles (Fine Science Tools) were passed through the genioglossus or intercostal muscles and secured with a knot (Pagliardini et al., 2011). Teflon was removed from a small (<0.5mm) segment of the wire adjacent to the knot, allowing the exposed wire to be embedded in the GG or intercostal muscles. The EMG electrodes were connected to an AC differential amplifier (A-M systems AM1800), band-pass filtered (300Hz/10kHz) and digitized with an PCI DAQ device (PCI NIDAQ 6251), along with USV and respiration measurements, allowing for synchronous data acquisition at 250kHz (single EMG) or 200kHz (dual EMGs). The EMG data was rectified and integrated offline with a modified Paynter filter in Matlab.

Laryngeal (TA) muscle lesion—Neonatal mice were anaesthetized by hypothermia and gently fixed in the supine position. A small 2mm incision was made ventrally in the neck, and the muscles overlying the thyroid cartilage were carefully isolated with sutures. A microincision was made on the thyroid cartilage with the sharp tip of a 28G needle, and a small bipolar electrode (Microprobes) was inserted into the TA muscle. The muscle was lesioned by passing a current of 500μA for 2.5-5 seconds. For the sham group, the same

protocol was followed except no current was passed after inserting the bipolar electrodes into the TA muscle. The neck was sutured, and mouse was allowed to recover fully before recording of attempted vocalizations. After the recording, the larynx was fully dissected to confirm the site of the lesion.

Stereotaxic electrolytic lesion, injection and stimulation—Bilateral stereotaxic injections and electrolytic lesions were performed in neonatal mice anaesthetized by hypothermia. The mouse was oriented on a stereotaxic frame (Kopf) with a neonatal adaptor (Stoelting) such that bregma was 1.5mm below lambda. In this position, the coordinates used for the iRO node were: P2: 2.50 mm posterior, 3.35 mm ventral from surface of the brain, $\pm$ 0.82 mm lateral from lambda; P3: 2.30 mm posterior, 3.50 mm ventral from surface of the brain, $\pm$0.87 mm lateral from lambda. Electrolytic lesions were performed with a concentric bipolar microelectrode (FHC) by passing a current of 30-80μA for 2-5 seconds. Animals were fully recovered on a heat pad and returned to their nest. After lesions, neonates recovered for at least 24 hours before breathing and vocalizations were recorded again. After the post lesion recordings were performed, lesion sites were validated by both anatomical localization visualized by light microscopy and changes of GCaMP6s activity in the iRO and preBötC in a medullary slice preparation (described below). Lesions were classified as bilateral "off" target from the iRO node, bilateral "on" target, or unilateral "on" target. Criteria used to classify lesions as "on" target: 1) immediately medial to the cNA (within 50-100μm), 2) dorsal to the BötC, 3) did not contain the cNA, and 4) the absence of the iRO rhythm in synaptic blockers measured by changes in GCaMP6s fluorescence, "off" target lesions were used as the control group and therefore all breathing, vocalization, and physiology validation were performed as a blinded study. The same coordinates were used for stereotaxic injection. Approximately 70nL of nifedipine (10μM), 70nL of carbenoxolone (1mM), or 70nL of ACSF were injected with a Nanoject III (Drummond), at a rate of 2-3nLs/second. The animals were recovered on a heating pad. Breathing and vocalization were recorded ~30 minutes after injection. Injection sites were confirmed by histological analysis of co-injected dye. For stimulation studies, a tungsten microelectrode (MicroProbes) was stereotaxically lowered into the iRO area and rigidly implanted using superglue. The animals were recovered on a heating pad for 30 minutes. Stimulation current (10ms train of biphasic current pulses at 400Hz: 0.4 ms pulse, 2.1ms between each pulse) was delivered via an isolated pulse stimulator (AM Systems). The stimulation intensity was gradually increased from 50μA to 600μA or until a phenotype was observed. The location of the electrode was verified histologically following each experiment.

***In vivo* optogenetics**—Neonatal mice were cryoanesthetized and positioned on the stereotaxic frame as described above. A single fiber optic ferrule and fiber (1.25mm ferrule, 200μm core fiber, Thorlabs) was lowered into the brain using the coordinates for the iRO node, positioned approximately 200μm above the iRO node. The ferrule was superglued in place on the skull, and the mice were allowed to recover on a heating pad for 30 minutes. Following recovery, the mouse was connected to a DPSS laser (532 nM, Shanghai Laser and Optics Co., ~20 mW) using patch cable (Doric lenses) and lowered into the chamber for recording. The laser was controlled by TTL Pulse Generator (Doric lenses). Single pulses were triggered near the peak of expiration using the PowerLab (ADInstruments)

fast response output connected to the TTL. Train of pulses were triggered randomly. All data was analyzed with a custom Matlab code to align pulses with ultrasonic sound and breathing.

Laryngeal Rabies virus and Cholera toxin injections—
Rabies tracing was performed using Chat-Cre;ROSA-LSL-G-TVA (Gt(ROSA)26Sor^tm1(CAG-RABVgp4,-TVA)Arenk) mice and the G-Deleted Rabies viruses listed above. For a subset of tracing experiments, a G-Deleted Rabies virus was coinjected with HSV hEF1a-Rabies G in C57Bl/6J or *Snap25*-Gcamp6s mice. Neonatal mice at P0 were cryoanesthetized and fixed in various positions with adhesive that were suitable for the muscle being injected. Each muscle was injected using a Nanoject III (Drummond). Between 30 to 150 nLs (depending on muscle) of virus were injected unilaterally, depending on the muscle, at a rate of 5-10nL/sec. Muscles injected were the cricothyroid, thyroarytenoid, genioglossus, masseter, whisker pad, and nose in order to trace the premotor neurons for vocalization (larynx, genioglossus), swallowing (genioglossus), chewing (masseter), and whisking (whiskers), and nose movement (nose). For injection into the laryngeal muscles (thyroarytenoid and cricothyroid), the overlaying muscles were bluntly dissected and carefully isolated with sutures. A microincision was made on the thyroid cartilage with the sharp tip of a 28G needle to allow for insertion of the micropipette into the thyroarytenoid muscle. Normal saline was used to flush the overlying area to prevent any nonspecific infection and labeling. After injections, the neonates were recovered on a heat pad and then returned to their nest. Neonates recovered for 4 days and then were euthanized for medullary slice preparation (described below). Rabies traced fluorescent neurons were identified and their electrophysiological activity was recorded. Cholera Toxin Subunit B (C34776, Life Technologies) injections were performed as described above, except they were only into the thyroarytenoid and cricothyroid muscles, and animals recovered for 2 days before euthanasia for brainstem slice preparation. All injection solutions contained fast-green dye to confirm that only the correct muscle was injected.

Histology—4-7 days after injection of the viral cocktail, pups were transcardially perfused with 10mL of heparinized saline followed by 10mL of 4% PFA in phosphate-buffered saline (PBS). The brains were dissected and postfixed overnight in 4% PFA, cryoprotected in 15 or 30% sucrose PBS (w/v) and embedded in OCT. The embedded brains were cryosectioned at 20 or 30μm. Sections were then blocked for 1 hour in 0.5% triton-X PBS and 4% normal horse or goat serum and subsequently incubated with a solution of primary antibodies in the blocking solution at 4°C overnight. For samples that required the use of a mouse primary antibody, the sections were further blocked using the Mouse on Mouse Blocking Reagent (Vector Labs, MKB-2213-1) for 1 hour prior to incubation in the primary antibody. The primary antibodies used are: chicken anti-GFP (Aves, GFP-1020), goat anti-ChAT (Millipore, AB144p), rabbit anti-GFP (Invitrogen, A11122), rabbit anti-phox2b (Jean-François Brunet lab), mouse anti-phox2b (Santa Cruz, B-11), rat anti-RFP (Chromotek, 5F8). The sections were washed in PBS, and the incubation procedure was then repeated with a solution containing secondary antibodies for 1-4 hours at 4°C. The secondary antibodies used are: donkey anti-chicken 488 (Jackson ImmunoResearch, 703-545-155), donkey anti-chicken Cy5 (Jackson ImmunoResearch, 703-176-155), donkey

Wei et al.

Page 16

anti-goat Cy5 (Jackson ImmunoResearch, 705-606-147), donkey anti-rabbit 488 (Jackson ImmunoResearch, 711-545-152) donkey anti-rabbit Cy5 (Jackson ImmunoResearch, 712-165-153), donkey anti-rat Cy3 (Jackson ImmunoResearch, 711-495-152), goat anti-mouse Alexa Fluor 647 (Invitrogen, 21236). The slides were washed in PBS, air dried and mounted using mowiol or fluorescence mounting medium (Dako) and coverslipped. Epifluorescence and confocal images were acquired with a NanoZoomer S210 digital slide scanner (Hamamatsu Photonics), Leica SP5 confocal microscope (Leica), or Nikon CSU-W1 Spinning Disk (Nikon). For RearChR+, only membrane-bound mCitrine were quantified.

Slice preparation and electrophysiology—550 to 650μm-thick transverse medullary slices which contain the preBötC and cranial nerve XII (XIIn) were prepared from neonatal P0-5 *Snap25*-GCaMP6s, *Chat-Cre*;ROSA-LSL-G-TVA (Gt(ROSA)26Sor[tm1(CAG-RABVgp4,-TVA)Arenk]) rabies injected, HSV and rabies injected, and lesioned animals were prepared as described (Ruangkittisakul et al., 2014). Briefly, slices were cut in ACSF containing (in mM): 124 NaCl, 3 KCl, 1.5 CaCl$_2$, 1 MgSO$_4$, 25 NaHCO$_3$, 0.5 NaH$_2$PO$_4$, and 30 D-glucose, equilibrated with 95% O$_2$ and 5% CO$_2$ (4°C, pH=7.4). The rostral side of the slice was taken 100μm caudal to the end of the facial nucleus, at the rostral end of the compact nucleus ambiguus. Note, these rostral boundaries are likely why the observed preBötC rhythm is slower than most other reports. All recordings were performed in the ACSF described above except the K$^+$ was raised to 9 mM, and osmotically balanced, and temperature was raised to 27.5-28.5°C. This elevation of extracellular K$^+$ enables spontaneous preBötC activity to activate the hypoglossal motor nucleus (Kam et al., 2013). The iRO neurons were identified by either monosynaptic rabies virus tracing from the thyroarytenoid muscle or by the presence of the iRO rhythm in *Snap25*-GCaMP6s mice (expiratory oscillation or gap-junction-dependent oscillation). If the neurons were identified without the cocktail of fast synaptic blockers, after each experiment the antagonists were applied to ensure the neuron contained the iRO signature rhythm (gap-junction-dependent oscillation). The preBötC neural activity was inferred by the activity recorded from either XIIn rootlet or as population activity directly from the XII motor nucleus using suction electrodes, amplified and low/high pass filtered at 3kHz/400Hz, rectified, integrated and digitized using Digidata 1550B. Current and voltage clamp recordings of single neurons were performed with a MultiClamp700A or B using pClamp9 and digitized at 10000 Hz. Internal consisted of K$^+$-Gluconate (135mM), EGTA (1.1mM), NaCl (5mM), CaCl$_2$ (0.1mM), HEPES (10mM), ATP (2mM), GTP (0.3mM). Alexa-488 was used to fill recorded neurons. For experiments in synaptic blockers, NBQX (10μM, Abcam, ab120046) or CNQX (10μM, Abcam, ab120044), D-APV (50μM, Alomone Labs, D-145), picrotoxin (100μM, Abcam, ab120315), strychnine (1μM, Sigma Aldrich, S0532) were bath applied after an initial 20-minute recovery period in 9mM K$^+$ ACSF. For pharmacological analysis of rhythmic activity, the following peptides and drugs were bath applied: Carbenoxolone (50-150μM, Sigma-Aldrich), 18ß-glycyrrhetinic acid (150μM, Sigma-Aldrich, G10105), Meclofenamic acid (100μM. Fisher Scientific, AAJ6048403), tetrodotoxin (TTX, 1μM, Abcam, ab120054), Substance P (200nM, Abcam, ab120170), DAMGO (20-200nM, Abcam, ab120674), Nifedipine (2μM, Tocris, 1075), Bay K8644 (100nM, Tocris, 154410), Veratridine (250nM, Abcam, ab120279), ZD7288

Neuron. Author manuscript; available in PMC 2023 February 16.

(100μM, Abcam, ab120102), Riluzole (20μM, Abcam, ab120272), Mibefradil (10μM, Tocris, 219810), Iberiotoxin (50nM, Alomone Labs, STI-400), UCL1684 (50nM, Tocris, 13105). For pharmacological analysis of rhythmic activity, the drugs were added to the internal recording solution: QX314 chloride (5mM, Tocris, 2313). For optogenetic studies, fluorescently tagged, membrane bound ReaChR-mCitrine neurons were recorded, and an LED (Excelitas) source was used to illuminate the neurons.

Gap junction electrical coupling—Gap junctions between the iRO neurons were validated by both electrical coupling. To determine if neurons were electrically coupled, the iRO neurons were identified by Snap25-GCaMP6s activity in 9mM K^+ ACSF containing synaptic blockers. After a pair of iRO neurons were patched, TTX was bath applied to silence the spontaneous rhythm. A current step of 500pA was applied to one neuron and a corresponding change in membrane potential was recorded. After, a similar current protocol was applied to the alternative neuron.

Quantification and statistical analysis

Statistics—Statistical tests were performed on data collected from electrolytic lesions, electrical stimulation, nifedipine, ACSF, and carbenoxolone stereotaxic injection, and optogenetic stimulation. For all datasets, a Shapiro-Wilks test was first performed to assess normality of the distribution. P-value <0.05. If both groups to be compared had normal distributions, a one tailed t-test with unequal variance was performed. If one or both datasets were not normal, then a Wilcox Rank Sum was performed. For electrolytic lesions, the t-test compared "off" target to bilateral "on" target lesions and "off" target to unilateral lesions. For pharmacology microinjections, ACSF was compared with nifedipine and carbenoxolone.

Supplementary Material

Refer to Web version on PubMed Central for supplementary material.

Acknowledgments:

References

Anderson TM, Garcia AJ, Baertsch NA, Pollak J, Bloom JC, Wei AD, Rai KG, and Ramirez JM (2016). A novel excitatory network for the control of breathing. Nature 536, 76–80. [PubMed: 27462817]

Bielle F, Griveau A, Narboux-Nême N, Vigneau S, Sigrist M, Arber S, Wassef M, and Pierani A (2005). Multiple origins of Cajal-Retzius cells at the borders of the developing pallium. Nature Neuroscience 8, 1002–1012. [PubMed: 16041369]

Chagnaud BP, Baker R, and Bass AH (2011). Vocalization frequency and duration are coded in separate hindbrain nuclei. Nature Communications 2, 346–11.

Daigle T, Madisen L, Hage T, Valley M, Knoblich U, Larsen R, Takeno M, Huang L, Gu H, and Larsen R et al. (2018). A Suite of Transgenic Driver and Reporter Mouse Lines with Enhanced Brain-Cell-Type Targeting and Functionality. Cell 174, 465–480.e22. [PubMed: 30007418]

Ehret G (2005). Infant Rodent Ultrasounds – A Gate to the Understanding of Sound Communication. Behavior Genetics 35, 19–29. [PubMed: 15674530]

French CR, Sah P, Buckett KJ, and Gage PW (1990). A voltage-dependent persistent sodium current in mammalian hippocampal neurons. The Journal of General Physiology 95, 1139–1157. [PubMed: 2374000]

Grillner S, El Marina A (2020) Current principles of motor control, with special reference to vertebrate locomotion. Physiological Reviews 100, 271–320 [PubMed: 31512990]

Hage SR (2009). Localization of the central pattern generator for vocalization. In Handbook of Mammalian Vocalization (Elsevier B.V.), pp. 329–337.

Harris JA, Hirokawa KE, Sorensen SA, Gu H, Mills M, Ng LL, Bohn P, Mortrud M, Ouellette B, Kidney J, et al. (2014). Anatomical characterization of Cre driver mice for neural circuit mapping and manipulation. Frontiers in Neural Circuits 8, 76. [PubMed: 25071457]

Hernandez-Miranda LR, Ruffault PL, Bouvier JC, Murray AJ, Morin-Surun MP, Zampieri N, Cholewa-Waclaw JB, Ey E, Brunet JF, Champagnat J, et al. (2017). Genetic identification of a hindbrain nucleus essential for innate vocalization. Proceedings of the National Academy of Sciences of the United States of America 114, 8095–8100. [PubMed: 28698373]

Hernández-Morato I, Pascual-Font A, Ramírez C, Matarranz-Echeverría J, Mchanwell S, Vázquez T, Sañudo JR, and Valderrama-Canales FJ (2013). Somatotopy of the Neurons Innervating the Cricothyroid, Posterior Cricoarytenoid, and Thyroarytenoid Muscles of the Rat's Larynx. The Anatomical Record 296, 470–479. [PubMed: 23381831]

Hippenmeyer S, Vrieseling E, Sigrist M, Portmann T, Laengle C, Ladle DR, and Arber S (2005). A Developmental Switch in the Response of DRG Neurons to ETS Transcription Factor Signaling. PLoS Biology 3, e159–13. [PubMed: 15836427]

Holy TE, and Guo Z (2005). Ultrasonic Songs of Male Mice. PLoS Biology 3, e386–10. [PubMed: 16248680]

Hooks B, Lin J, Guo C, and Svoboda K (2015). Dual-Channel Circuit Mapping Reveals Sensorimotor Convergence in the Primary Motor Cortex. Journal Of Neuroscience 35, 4418–4426. [PubMed: 25762684]

Huckstepp RT, Henderson LE, Cardoza KP, and Feldman JL (2016). Interactions between respiratory oscillators in adult rats. ELife 5, e14203. [PubMed: 27300271]

Jean A (2001). Brain stem control of swallowing: neuronal network and cellular mechanisms. Physiological Reviews 81, 929–969. [PubMed: 11274347]

Johnson AM, Ciucci MR, Russell JA, Hammer MJ, and Connor NP (2010). Ultrasonic output from the excised rat larynx. The Journal of the Acoustical Society of America 128, EL75–EL79. [PubMed: 20707418]

Kakizaki T, Sakagami H, Sakimura K, and Yanagawa Y (2017). A glycine transporter 2-Cre knock-in mouse line for glycinergic neuron-specific gene manipulation. IBRO Reports 3, 9–16. [PubMed: 30135938]

Kam K, Worrell JW, Janczewski WA, Cui Y, and Feldman JL (2013). Distinct inspiratory rhythm and pattern generating mechanisms in the preBötzinger complex. Journal of Neuroscience 33, 9235–9245. [PubMed: 23719793]

Kaupp UB, and Seifert R (2001). Molecular diversity of pacemaker ion channels. Annual Review of Physiology 63, 235–257.

Kurnikova A, Deschênes M, and Kleinfeld D (2019). Functional brain stem circuits for control of nose motion. Journal of Neurophysiology 121, 205–217. [PubMed: 30461370]

Lim R, Zavou MJ, Milton P-L, Chan ST, Tan JL, Dickinson H, Murphy SV, Jenkin G, and Wallace EM (2014). Measuring respiratory function in mice using unrestrained whole-body plethysmography. Journal of Visualized Experiments: JoVE e51755. [PubMed: 25146417]

Long EC, and Hull WE (1961). Respiratory volume-flow in the crying newborn infant. Pediatrics 27, 373–377. [PubMed: 13763319]

Luschei ES, Ramig LO, Finnegan EM, Baker KK, and Smith ME (2006). Patterns of laryngeal electromyography and the activity of the respiratory system during spontaneous laughter. Journal of Neurophysiology 96, 442–450. [PubMed: 16772517]

Madisen L, Garner AR, Shimaoka D, Chuong AS, Klapoetke NC, Li L, van der Bourg A, Niino Y, Egolf L, Monetti C, et al. (2015). Transgenic Mice for Intersectional Targeting of Neural Sensors and Effectors with High Specificity and Performance. Neuron 85, 942–958. [PubMed: 25741722]

Mahrt E, Agarwal A, Perkel D, Portfors C, and Elemans CPH (2016). Mice produce ultrasonic vocalizations by intra-laryngeal planar impinging jets. Current Biology 26, 1–2. [PubMed: 26725201]

Marder E, and Bucher D (2001). Central pattern generators and the control of rhythmic movements. Curr Biol 11, R986–R996. [PubMed: 11728329]

Milstein AD, Bloss EB, Apostolides PF, Vaidya SP, Dilly GA, Zemelman BV, and Magee JC (2015). Inhibitory Gating of Input Comparison in the CA1 Microcircuit. Neuron 87, 1274–1289. [PubMed: 26402609]

Moore JD, Deschênes M, Furuta T, Huber D, Smear MC, Demers M, and Kleinfeld D (2013). Hierarchy of orofacial rhythms revealed through whisking and breathing. Nature 497, 205–210. [PubMed: 23624373]

Mortola JP, and Frappell PB (1998). On the barometric method for measurements of ventilation, and its use in small animals. Can J Physiol Pharm 76, 937–944.

Del Negro CA, Funk GD, and Feldman JL (2018). Breathing matters. Nature Reviews Neuroscience 254, 1–17.

Okubo TS, Mackevicius EL, Payne HL, Lynch GF, and Fee MS (2015). Growth and splitting of neural sequences in songbird vocal development. Nature 528, 352–357. [PubMed: 26618871]

Pagliardini S, Janczewski WA, Tan W, Dickson CT, Deisseroth K, and Feldman JL (2011). Active Expiration Induced by Excitation of Ventral Medulla in Adult Anesthetized Rats. Journal of Neuroscience 31, 2895–2905. [PubMed: 21414911]

Patrickson JW, Smith TE, and Zhou SS (1991). Motor neurons of the laryngeal nerves. The Anatomical Record 230, 551–556. [PubMed: 1718189]

Pattyn A, Hirsch M, Goridis C, and Brunet JF (2000). Control of hindbrain motor neuron differentiation by the homeobox gene Phox2b. Development 127, 1349–1358. [PubMed: 10704382]

Plummer NW, Evsyukova IY, Robertson SD, de Marchena J, Tucker CJ, & Jensen P (2015). Expanding the power of recombinase-based labeling to uncover cellular diversity. Development, 142(24), 4385–4393. [PubMed: 26586220]

Poeppel D, and Assaneo MF (2020). Speech rhythms and their neural foundations. Nature Reviews Neuroscience 1–13. [PubMed: 31796912]

Pomberger T, Risueno-Segovia C, Löschner J, and Hage SR (2018). Precise Motor Control Enables Rapid Flexibility in Vocal Behavior of Marmoset Monkeys. Current Biology 28, 788–794. [PubMed: 29478857]

Prescott SL, Umans BD, Williams EK, Brust RD, and Liberles SD (2020). An Airway Protection Program Revealed by Sweeping Genetic Control of Vagal Afferents. Cell 181, 574–589. [PubMed: 32259485]

Riede T (2014). Rat ultrasonic vocalization shows features of a modular behavior. Journal of Neuroscience 34, 6874–6878. [PubMed: 24828641]

Riede T (2018). Peripheral Vocal Motor Dynamics and Combinatory Call Complexity of Ultrasonic Vocal Production in Rats (Elsevier B.V.).

Rossi J, Balthasar N, Olson D, Scott M, Berglund E, Lee CE, Choi MJ, Lauzon D, Lowell BB, and Elmquist JK (2011). Melanocortin-4 receptors expressed by cholinergic neurons regulate energy balance and glucose homeostasis. Cell Metabolism 13, 195–204. [PubMed: 21284986]

Rousso DL, Qiao M, Kagan RD, Yamagata M, Palmiter RD, and Sanes JR (2016). Two Pairs of ON and OFF Retinal Ganglion Cells Are Defined by Intersectional Patterns of Transcription Factor Expression. CellReports 15, 1930–1944.

Ruangkittisakul A, Kottick A, Picardo MCD, Ballanyi K, and Del Negro CA (2014). Identification of the pre-Botzinger complex inspiratory center in calibrated "sandwich" slices from newborn mice with fluorescent Dbx1 interneurons. Physiological Reports 2, e12111–e12111. [PubMed: 25138790]

Schwab MH, Bartholomae A, Heimrich B, Feldmeyer D, Druffel-Augustin S, Goebbels S, Naya FJ, Zhao S, Frotscher M, Tsai MJ, et al. (2000). Neuronal basic helix-loop-helix proteins (NEX and BETA2/Neuro D) regulate terminal granule cell differentiation in the hippocampus. Journal of Neuroscience 20, 3714–3724. [PubMed: 10804213]

Sherman D, Worrell JW, Cui Y, and Feldman JL (2015). Optogenetic perturbation of preBötzinger complex inhibitory neurons modulates respiratory pattern. Nature Neuroscience 18, 408–414. [PubMed: 25643296]

Smith JC, Ellenberger HH, Ballanyi K, Richter DW, and Feldman JL (1991). Pre-Bötzinger complex: a brainstem region that may generate respiratory rhythm in mammals. Science 254, 726–729. [PubMed: 1683005]

Srinivas S, Watanabe T, Lin CS, William CM, Tanabe Y, Jessell TM, and Costantini F (2001). Cre reporter strains produced by targeted insertion of EYFP and ECFP into the ROSA26 locus. Bmc Dev Biol 1, doi:10.1186/1471-213x-1-4.

Stanek E, Cheng S, Takatoh J, Han BX, and Wang F (2014). Monosynaptic premotor circuit tracing reveals neural substrates for oro-motor coordination. ELife 3, e02511. [PubMed: 24843003]

Takatoh J, Nelson A, Zhou X, Bolton MM, Ehlers MD, Arenkiel BR, Mooney R, and Wang F (2013). New modules are added to vibrissal premotor circuitry with the emergence of exploratory whisking. Neuron 77, 346–360. [PubMed: 23352170]

Taniguchi H, He M, Wu P, Kim S, Paik R, Sugino K, Kvitsiani D, Kvitsani D, Fu Y, Lu J, et al. (2011). A resource of Cre driver lines for genetic targeting of GABAergic neurons in cerebral cortex. Neuron 71, 995–1013. [PubMed: 21943598]

Tasic B, Yao Z, Graybuck LT, Smith KA, Nguyen TN, Bertagnolli D, Goldy J, Garren E, Economo MN, Viswanathan S, et al. (2018). Shared and distinct transcriptomic cell types across neocortical areas. Nature 563, 72–78. [PubMed: 30382198]

Titze IR, Finnegan EM, Laukkanen A-M, Fuja M, and Hoffman H (2008). Laryngeal muscle activity in giggle: a damped oscillation model. Journal of Voice 22, 644–648. [PubMed: 17509825]

Toor RUAS, Sun QJ, Kumar NN, Le S, Hildreth CM, Phillips JK, and McMullan S (2019). Neurons in the Intermediate Reticular Nucleus Coordinate Postinspiratory Activity, Swallowing, and Respiratory-Sympathetic Coupling in the Rat. Journal of Neuroscience 39, 9757–9766. [PubMed: 31666354]

Tschida K, Michael V, Takato J, Han B-X, Zhao S, Sakurai K, Mooney R, and Wang F (2019). A Specialized Neural Circuit Gates Social Vocalizations in the Mouse. Neuron 103, 459–472. [PubMed: 31204083]

Voiculescu O, Charnay P, and Schneider-Maunoury S (2000). Expression pattern of a Krox-20/Cre knock-in allele in the developing hindbrain, bones, and peripheral nervous system. Genesis 26, 123–126. [PubMed: 10686605]

Vong L, Ye C, Yang Z, Choi B, Chua S, and Lowell BB (2011). Leptin action on GABAergic neurons prevents obesity and reduces inhibitory tone to POMC neurons. Neuron 71, 142–154. [PubMed: 21745644]

Wilder CN (1974). Respiratory patterns in infant cry. Human Communication Winter 18–34.

Yamanishi T, Koizumi H, Navarro MA, Milescu LS, and Smith JC (2018). Kinetic properties of persistent Na+ current orchestrate oscillatory bursting in respiratory neurons. The Journal of General Physiology 150, 1523–1540. [PubMed: 30301870]

Zhang YS, and Ghazanfar AA (2020). A Hierarchy of Autonomous Systems for Vocal Production. Trends in Neurosciences 43, 1–12. [PubMed: 31744630]

Highlights

- Innate speech is a stereotyped rhythmic behavior predicted to be driven by a CPG

- Like speech, mouse cries have rhythmic syllables and a stereotyped motor program

- The iRO has the connectivity and intrinsic rhythmicity to produce timed cries

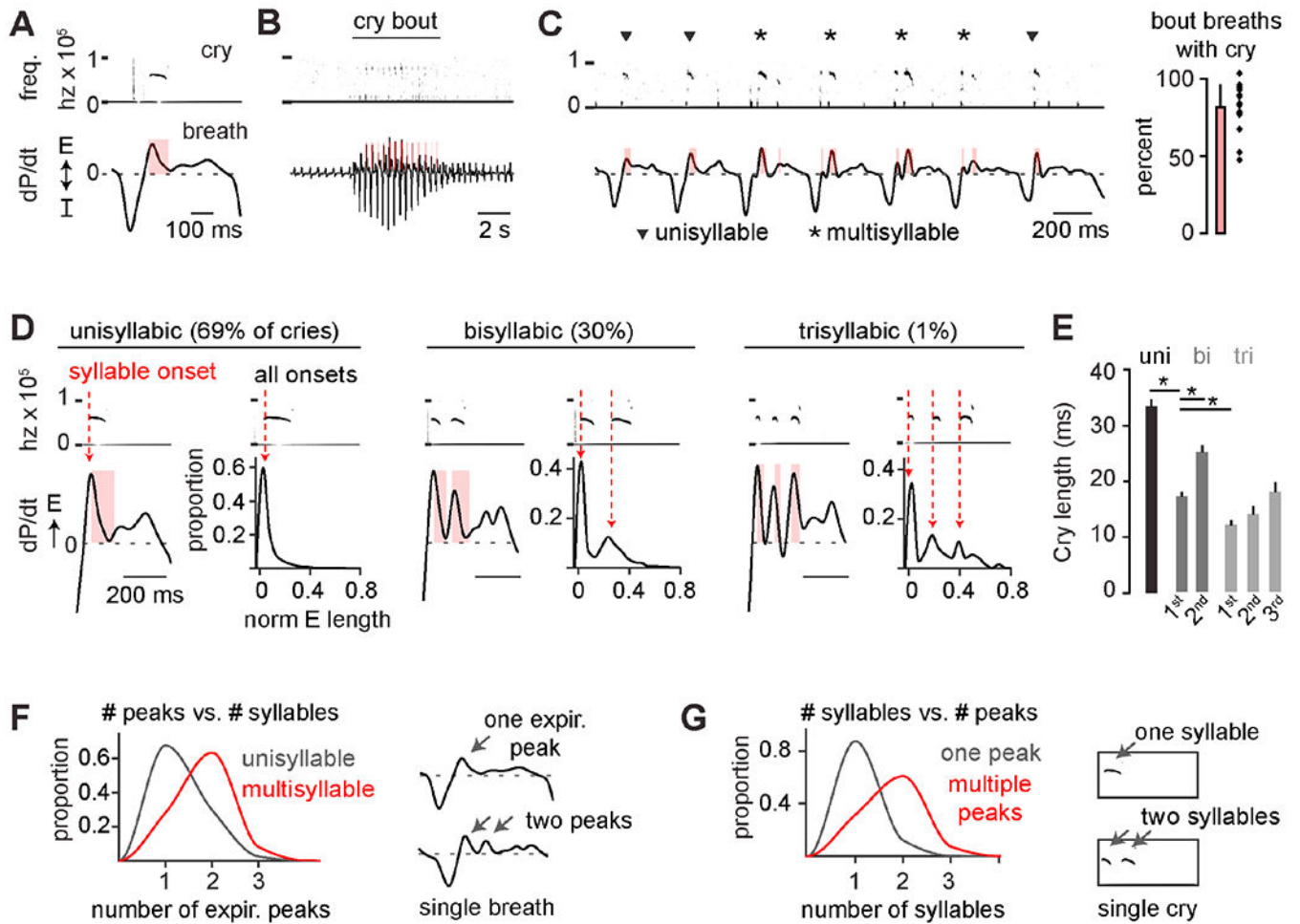- The iRO is necessary and sufficient for cries and the embedded syllable structure

Figure 1. Neonatal cries comprise syllables that are rhythmically timed within a breath.
A, Example cry breath with cry frequency spectrogram (0-100 kHz) and breath pressure changes (dP/dt, arbitrary units). E and I, expiration and inspiration. Red bar, USV length. **B**, Example large breaths during a cry bout and surrounding basal breaths. **C**, Cry bout in **B** with four multi- (*) and three unisyllabic (▾) cries. Right, percent cry bout breaths with USV (n = 17 mice, mean±SD). **D**, Left, examples of expiratory airflow when one, two, or three syllables are within a breath. Right, histograms of cry onset normalized to expiratory duration (n = 5596 cries, 23 mice). **E**, Syllable length for uni-, bi-, and trisyllabic cries. *, one-sided t-test p < 0.05. **F**, Proportion of expiratory peaks in cry breaths with one (uni-) versus two or more (multisyllable) cries (n = 11,186 breaths, 30 mice). **G**, As in **F**, but the proportion of syllables with one or multiple expiratory airflow peaks.
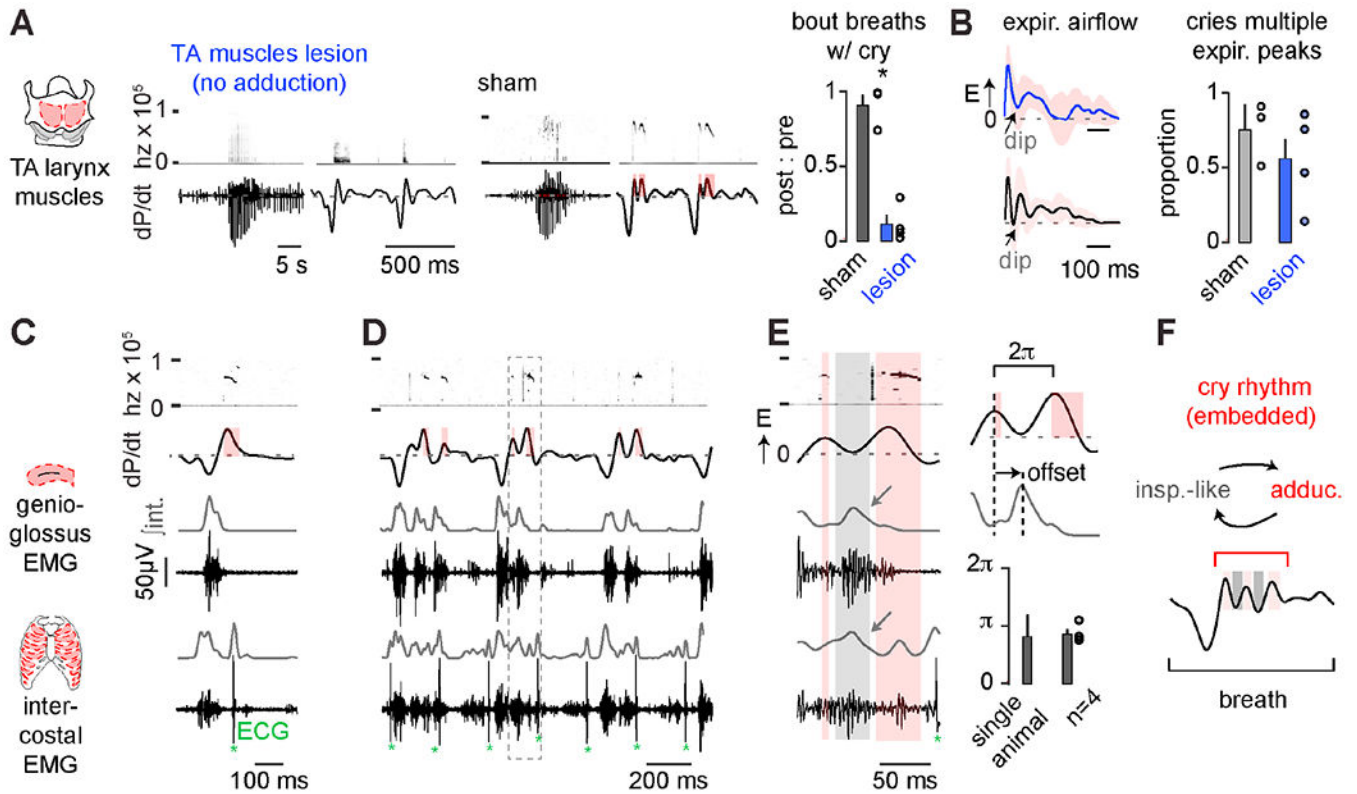
Figure 2. Cry syllables are synchronized with the respiratory motor program.
A, Example cry bout and breaths after bilateral TA muscle (left) or sham (middle) lesion. Right, number of cry bout breaths with cries in post- vs. pre-surgery (ratio of post : pre). Sham, black, n = 3; TA lesion, red, n = 4; mean ± SEM. *, one-sided Wilcoxon rank sum p < 0.05. **B**, avg. ± SD of cry breath expiratory airflow after TA lesion (47 lesion breaths, 26 sham) and proportion of cry breaths with multiple expiratory airflow peaks (mean ± SEM, 70-100 breaths analyzed per animal). **C**, Electromyographic (EMG) activity of the genioglossus (n = 4) and intercostal (n=5) inspiratory muscles. Gray, integrated (∫int.) activity. Example unisyllabic cry and associated inspiratory muscle activity. *denotes contaminating cardiac ECG signals. **D**, Example multisyllabic cries with additional inspiratory activity during expiratory airflow dips. **E**, Multisyllabic cry breath from boxed region in **D** showing coinciding genioglossus and intercostal muscle activity during the airflow dip. Timing of peak genioglossus activity compared to the local expiratory airflow peaks. **F**, Schematic showing re-cycling of inspiratory and laryngeal muscle activity during expiration to produce multisyllabic cries. See also Figures S1 and S2.
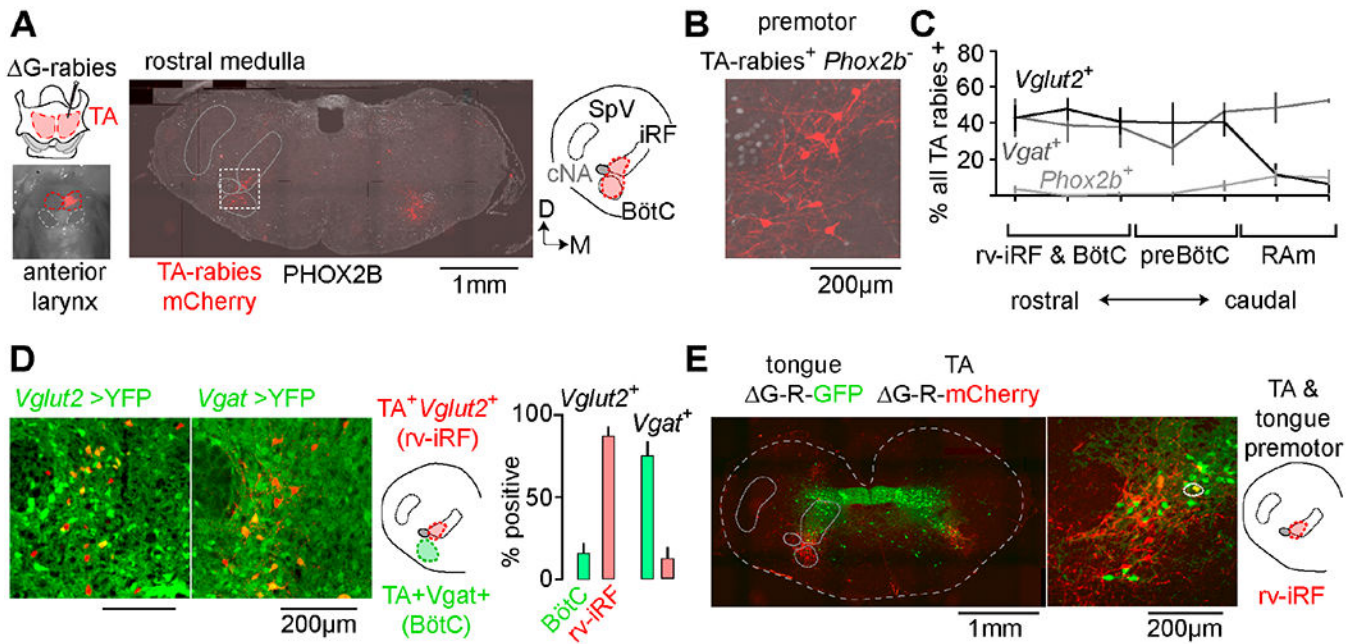
Figure 3. The medullary brainstem contains a cluster of premotor neurons for sound production and articulation.

A, Modified rabies (G-Rabies-mCherry) and helper (HSV-G) viruses co-injected into TA muscle. Middle, coronal section of rostral medulla showing distribution of rabies-mCherry$^+$ TA premotor neurons (red) and *Phox2b* (gray). Right, schematic illustrating the position of the intermediate reticular formation (iRF) and BötC, cNA, and spinal trigeminal nucleus (SpV). Dorsal; Medial. **B**, Boxed area in **A** showing a TA premotor neuron cluster (*Phox2b*-neg.) directly medial to cNA. **C**, Quantification of mean % ± SEM of rabies$^+$ neurons that were *Vglut2*$^+$ (black, n=3), *Vgat*$^+$ (gray, n=3), or *Phox2B*$^+$ (TA motor, pale gray, n=6) across the breathing control centers (rv-iRF/BötC, preBötC, and RAm). **D**, rv-iRF and BötC TA premotor neurons in *Vglut2*-Cre→YFP (n=3) and *Vgat*-Cre→YFP mice (n=3). Those medial to cNA are *Vglut2*$^+$ (rv-iRF) and in BötC are *Vgat*$^+$. Right, quantification. **E**, Coronal section showing the distribution of G-rabies-mCherry TA premotor neurons and G-rabies-GFP tongue premotor neurons. Middle, magnification of rv-iRF showing spatial overlap of premotor neurons. Circled neuron is double positive. See also Figures S3 and S4.
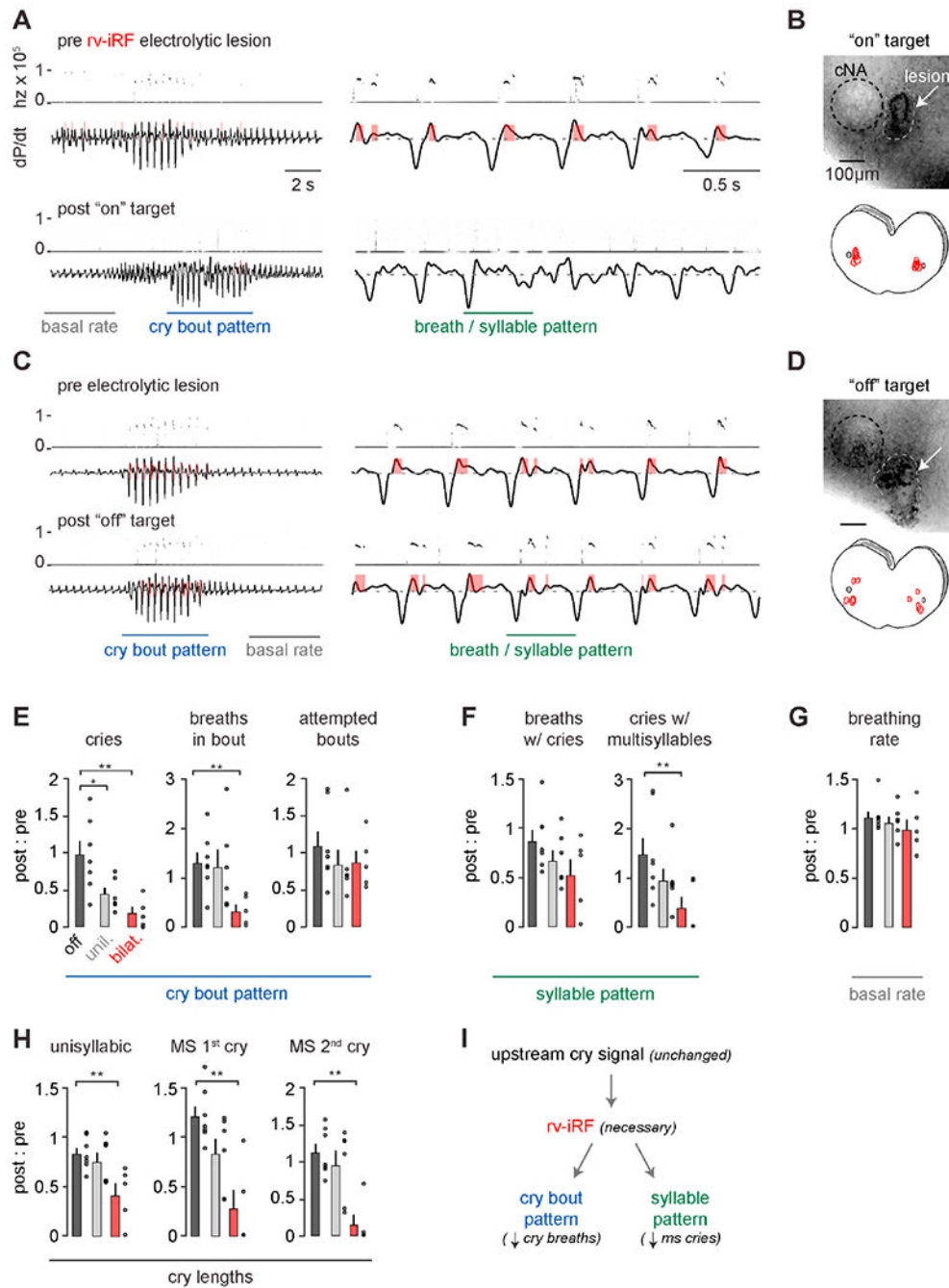
Figure 4. The rv-iRF premotor cluster is required for neonatal crying but not breathing.
A, Cry bout and breathing pattern before (top) and after (bottom) bilateral on-target electrolytic lesion of rv-iRF medial to cNA. **B**, Top, representative image of the lesion. Bottom, summary of locations for on-target lesions (n=5). **C-D**, As in **A-B** but for off-target lesions (n=7). **E**, Quantification of number of cry bouts and breaths and cries within them following bilateral on- (bilat.), unilateral on- (unil., n=6), and off-target (off) electrolytic lesions. Each parameter is a ratio of post-lesion : pre-lesion. Parameters include: total number of uni- and multisyllabic (MS) cries (p = 0.002), number of cry breaths per bout (p

= 0.002), and number of bouts in 5 minutes (p = 0.2). **F**, As in **E.** Parameters represent cry breath feature: the number of large breaths in a bout with a USV (p = 0.08), proportion of cries that are MS (p = 0.006). **G**, Basal respiratory rate (p = 0.1). **H**, Length of each cry syllable (p = 0.01, 0.004, 0.002). Data are mean ± SEM. One-sided t-test or Wilcoxon rank sum p < 0.05 (*) and < 0.01 (**). **I**, Model showing necessity of rv-iRF to pattern cry bouts and cry breaths. See also Figure S1.
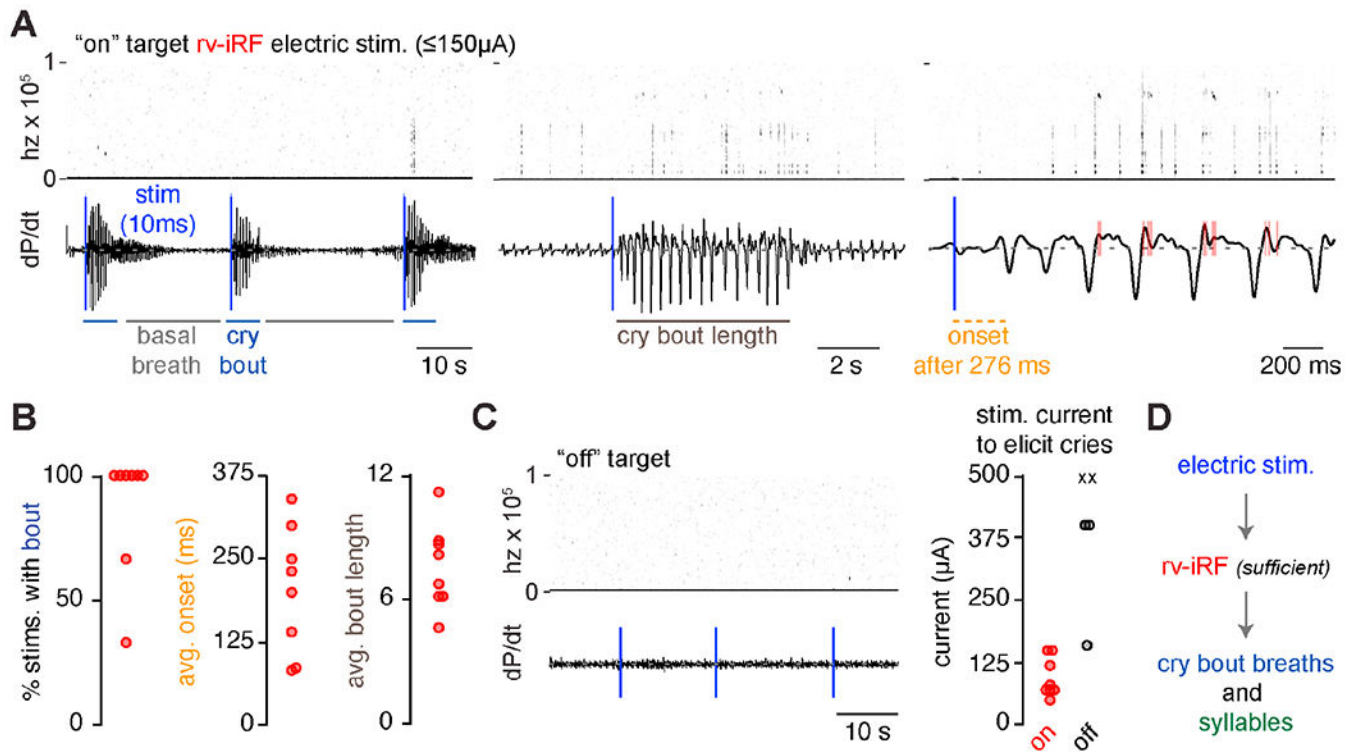
Figure 5. The rv-iRF is sufficient for neonatal crying.
A, Audio and airflow recordings with unilateral on-target 10ms electrical stimulations (4 x 0.4ms biphasic pulses). Blue vertical line indicates 10ms stimulation. **B**, Quantification of the percent of on-target stimulations that triggered a cry bout, average time to cry bout onset after stimulation, and average bout length. **C**, Audio and airflow recordings with three 10ms electrical stimulations with off-target electrical stimulation. Right, current (μA) required to initiate a cry bout when on (red circle, n=8 animals) or off-target (black circle or X, n=5). X, denotes animals where currents up to 600μA failed to elicit cries (n=2). **D**, Model showing the rv-iRF is sufficient to induce the entirety of a cry bout.
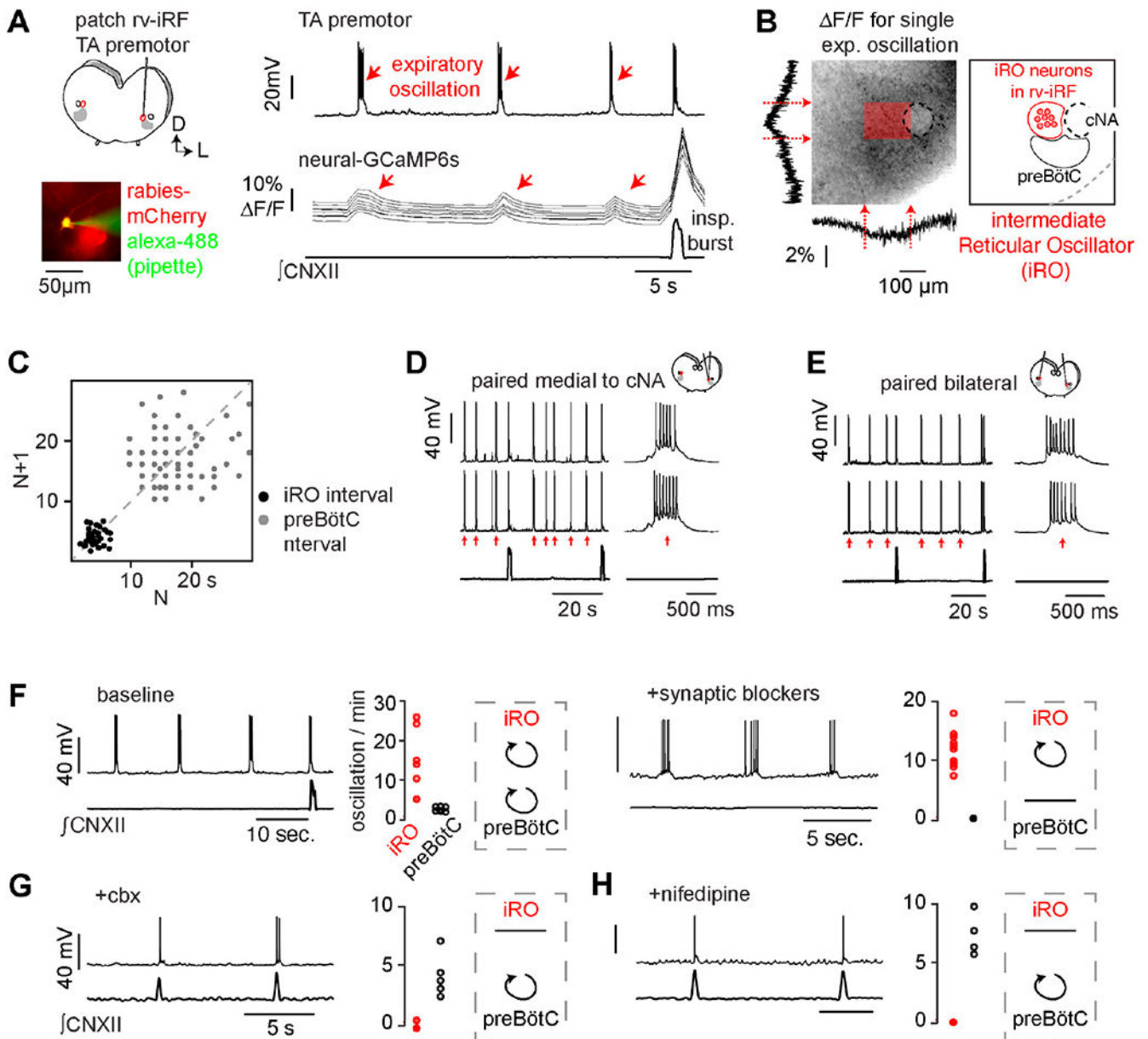
Figure 6. A novel *in vitro* oscillator in the rv-iRF is active during expiration.
A, Left, medullary *in vitro* slice preparation. G-rabies-mCherry TA premotor neurons in rv-iRF recorded using patch clamp (bottom, filled with Alexa-488 from pipette). Right, current clamp (I$_c$) recording of TA premotor rv-iRF neuron (n = 17/20), F/F in 10 neurons (*Snap25*-GCaMP6s), and ∫CNXII. Red arrows indicate expiratory oscillation. **B**, F/F summed vertically and horizontally during a single expiratory oscillation (dashed box, left). Max F/F localizes to dozens of neurons medial to cNA, denoted by shaded red box, which we named the iRO. **C**, Left, Poincaré plot of iRO (black) and preBötC (gray) intervals. **D**, Paired I$_c$ recordings of rv-iRF neurons medial to cNA. **E**, As in **D** but bilateral. **F**, I$_c$ recording of iRO neuron and ∫CNXII and number of oscillations per minutes (n=6 slices) before (left) and after bath applied blockers of fast synaptic neurotransmission (10μM

NBQX, 50μM APV, 100μM Picrotoxin, 1μM Strychnine, n=10) (Right). **G-H**, As in **F**, but after bath application of 50μM carbenoxolone (**G**, n=5) or 2 μM nifedipine (**H**, n=4). See also Figures S5, S6, S7.
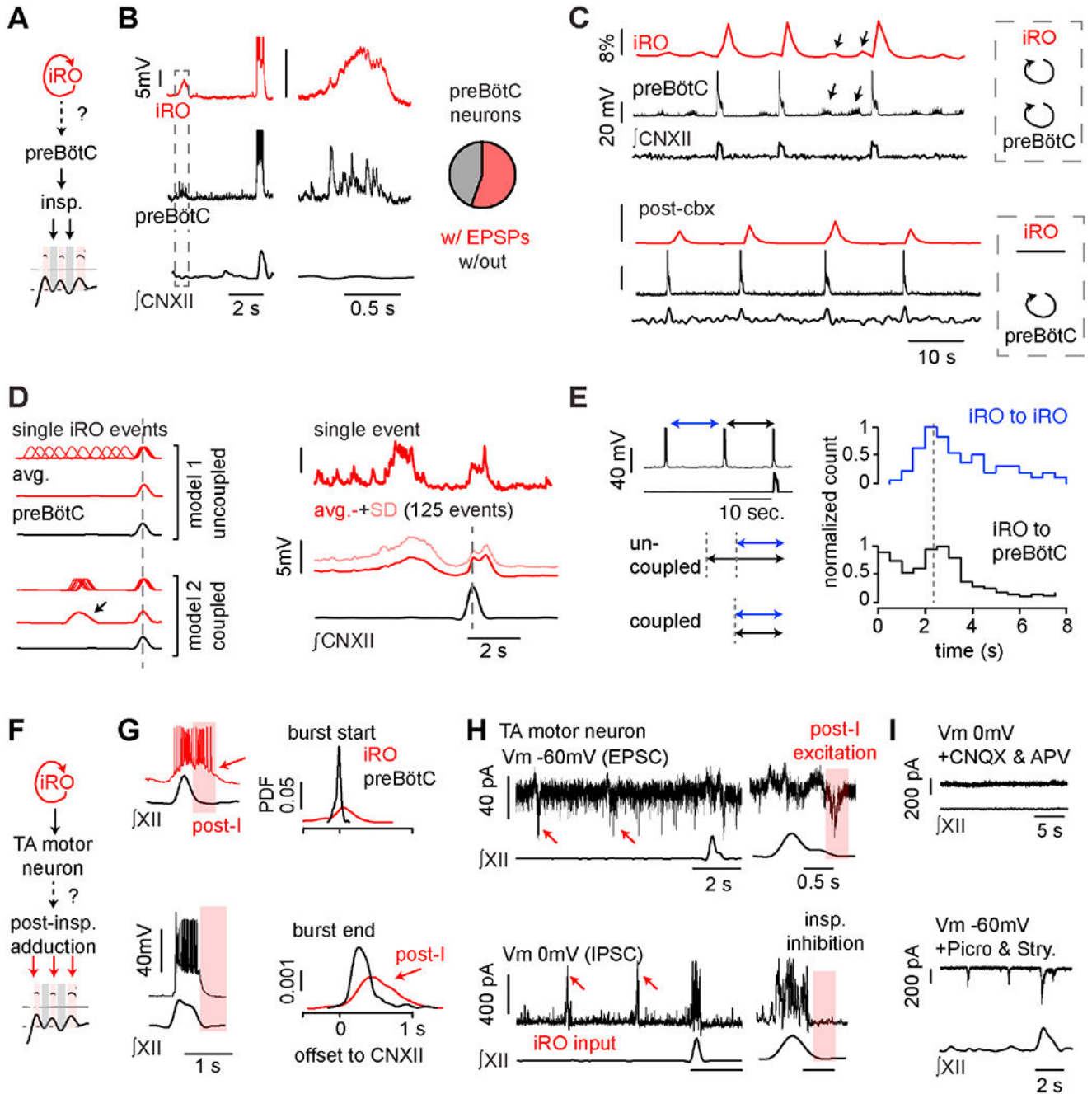
Figure 7. The iRO uses synaptic and functional connections to produce the cry motor program.
A, Schematic of how iRO might control inspiration (model from Figure 2). **B**, Paired
I_c recordings of iRO and preBötC inspiratory neurons (n = 5/11 paired recordings).
Right, magnification showing EPSPs in preBötC inspiratory neurons during iRO expiratory
oscillation. **C**, F/F in dozens of iRO neurons (*Snap25*-GCaMP6s), I_c recording preBötC
inspiratory neurons with ∫CNXII before (top) and after (bottom) bath application of the
iRO rhythm antagonist cbx. **D**, Left, schematic of the iRO and preBötC bursting if the two
rhythms are uncoupled vs. coupled. Right, 15 second iRO I_c recording and bottom, avg.

membrane potential ± SD for 125 events aligned to ∫CNXII peak. Action potentials were removed to visualize membrane potential oscillations. **E**, Left, schematic showing segments measured: blue - intervals between expiratory iRO oscillations, black - last iRO oscillation to preBötC burst. Right, histogram of duration of each segment (black: n = 182 events, blue: n=715 events). Data from 13 mice. **F**, Schematic of iRO induction of post-inspiratory laryngeal adduction (model from Figure 2). **G**, Example of iRO (red) and preBötC (black) bursts with ∫CNXII activity. iRO activity persists into post-inspiration. Right, probability density function of burst start and end compared to peak ∫CNXII activity (n = 7 iRO and 12 preBötC neurons). **H**, TA motor neurons identified by intramuscular injection of cholera toxin B-555. Top, example excitatory post-synaptic currents (EPSCs) in 13/22 motor neurons held at −60 mV. Bottom, example inhibitory post-synaptic currents (IPSCs) in 22/23 motor neurons held at a membrane potential (V_m) of 0 mV. Both input types coincide with iRO oscillations and EPSCs are post-inspiratory. **I**, Top, IPSCs are absent in CNQX and APV (V_m, 0 mV). Bottom, post-inspiratory EPSCs are now associated with inspiration in picrotoxin and strychnine (V_m, −60 mV), mirroring iRO activity. See also Figure S7.
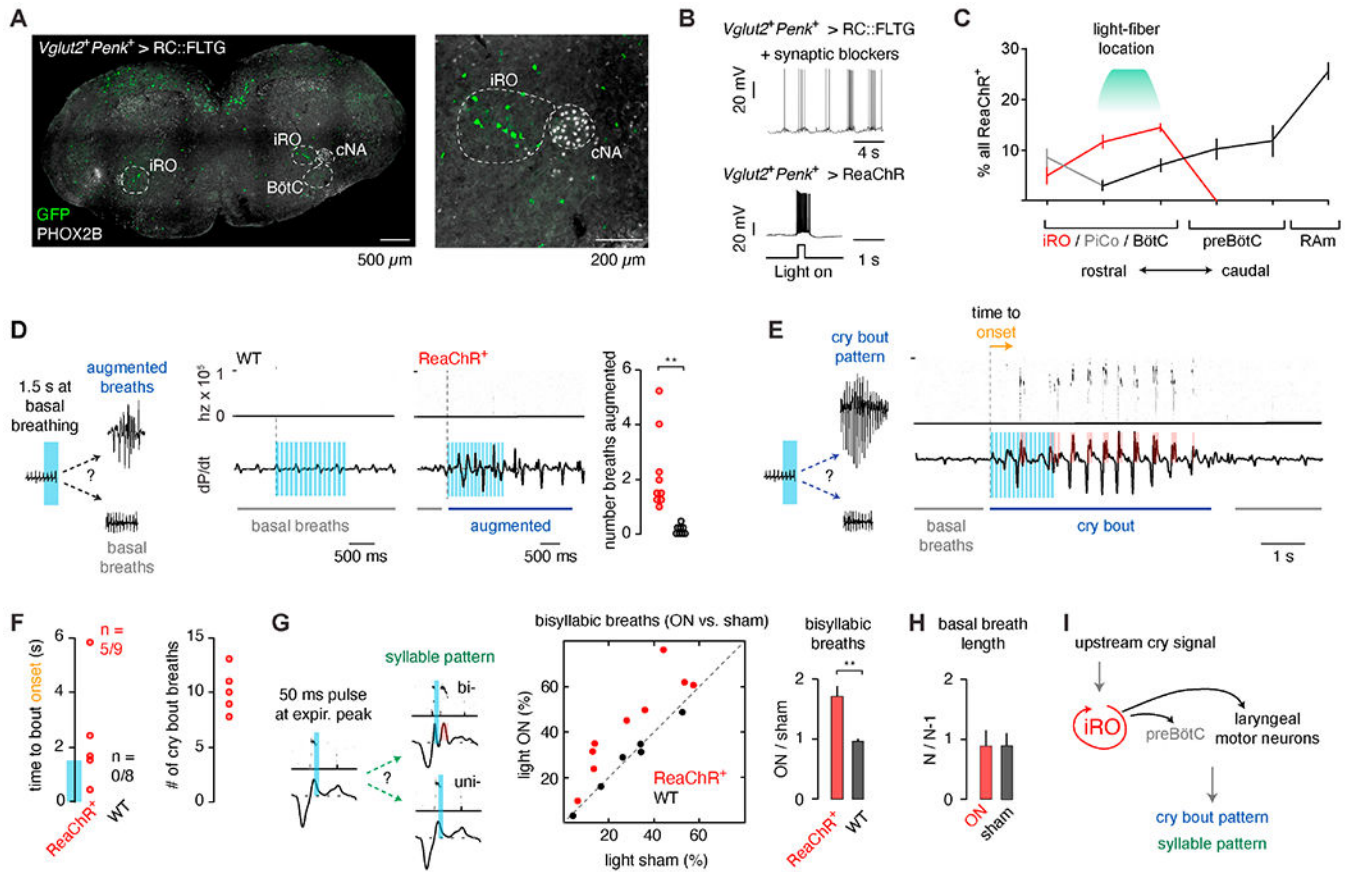
Figure 8. The iRO is sufficient to induce neonatal cry bouts and the cry syllables within a breath. **A**, *Vglut2*-Flp *Penk*-Cre expression of GFP in the RC::FLTG transgene (Flp + Cre > GFP). Coronal section of medulla showing GFP$^+$ neurons (green) and *Phox2b* expression (gray). Right, magnification of annotated area. **B**, Top, I$_c$ recording of a GFP$^+$ neuron (*Vglut2*$^+$*Penk*$^+$ > GFP) in fast synaptic blockers shows the hallmark iRO rhythm (n = 5/7). Bottom, I$_c$ recording of ReaChR$^+$ iRO neuron (*Vglut2*$^+$*Penk*$^+$ > ReaChR) with brief light illumination. **C**, Quantification of the proportion of all ReaChR$^+$ neurons (percent ± SEM) that localize to the iRO (red), PiCo (gray- *ChAT* positive), and BötC, preBötC, and RAm (black) (n=3). **D**, Representative change in breathing after 1.5 seconds 10Hz unilateral illumination of the iRO in ReaChR$^+$ or wildtype (control) neonatal mice. Average number of augmented breaths in each animal (9 ReaChR$^+$, 8 wildtype). **E**, As in **D**, representative change from basal breathing to complete cry bout in 5/9 ReaChR$^+$ animals. **F**, Left, time to cry bout onset. Note, no cry bouts were induced in wildtype. Blue bar on y-axis indicates the duration of laser stimulation. Right, average stimulated cry bout length in ReaChR$^+$ animals. **G**, Comparison of the percent of cries that show multiple syllables or expiratory airflow peaks that accompany each syllable without light (sham, OFF) versus with light (ON) in ReaChR$^+$ and wildtype controls. Right, mean ± SEM of ON : OFF. **H**, Basal breath length with 50ms light pulse (N) normalized to the length of the preceding breath (N-1) for breaths with light (ON) and sham. One-sided t-test or Wilcoxon rank sum P < 0.01 (**). **I**, Model

indicating that the iRO is sufficient to induce both the entirety of a cry bout and cry syllables in a breath. See also Figure S8 and Table S1.

Wei et al.

Page 34

KEY RESOURCES TABLE

REAGENT or RESOURCE	SOURCE	IDENTIFIER
Antibodies		
chicken anti-GFP	Aves	GFP-1020, RRID:AB_10000240
goat anti-ChAT	Millipore	AB144p, RRID:AB_2079751
rabbit anti-GFP	Invitrogen	A11122, RRID:AB_221569
rabbit anti-phox2b	Jean-François Brunet lab	N/A
mouse anti-phox2b	Santa Cruz Biotechnology	B-11, sc-376997, RRID:AB_2813765
rat anti-RFP	Chromotek	5F8, RRID:AB_2336064
donkey anti-chicken 488	Jackson ImmunoResearch	703-545-155, RRID:AB_2340375
donkey anti-chicken Cy5	Jackson ImmunoResearch	703-175-155, RRID:AB_2340365
donkey anti-goat Cy5	Jackson ImmunoResearch	705-606-147, RRID:AB_2340438
donkey anti-rabbit 488	Jackson ImmunoResearch	711-545-152, RRID:AB_2313584
donkey anti-rabbit Cy5	Jackson ImmunoResearch	712-165-153, RRID:AB_10895300
donkey anti-rat Cy3	Jackson ImmunoResearch	711-495-152, RRID:AB_92645
goat anti-mouse Alexa Fluor 647	Invitrogen	21236, RRID:AB_2535805
Bacterial and virus strains		
oG SiR G-Deleted Rabies-FlpO-mCherry	The Viral Vector Core at the Salk Institute for Biological Sciences	N/A
G-Deleted Rabies-eGFP	Janelia Viral Tools	N/A
G-Deleted Rabies-mCherry	Janelia Viral Tools	N/A
HSV-hEF1a-Rabies G	Gene Delivery Technology Core Massachusetts General Hospital	RN700
HSV-hCMV-YTB	Gene Delivery Technology Core Massachusetts General Hospital	N/A
Chemicals, peptides, and recombinant proteins		
Carbenoxolone	Sigma-Aldrich	C4790
18ß-glycyrrhetinic acid	Sigma-Aldrich	G10105
Meclofenamic acid	Fisher Scientific	AAJ6048403
Tetrodotoxin	Abcam	ab120054
Substance P	Abcam	ab120170
DAMGO	Abcam	ab120674
Nifedipine	Tocris	1075
Bay K8644	Tocris	154410
Veratridine	Abcam	ab120279
ZD7288	Abcam	ab120102
Riluzole	Abcam	ab120272
Mibefradil	Tocris	219810
Iberiotoxin	Alomone Labs	STI-400
UCL1684	Tocris	13105

Neuron. Author manuscript; available in PMC 2023 February 16.

REAGENT or RESOURCE	SOURCE	IDENTIFIER
QX314 chloride	Tocris	2313
NBQX	Abcam	ab120046
CNQX	Abcam	ab120044
D-APV	Alomone Labs	D-145
Picrotoxin	Abcam	ab120315
Strychnine	Sigma Aldrich	S0532
Cholera Toxin Subunit B, Alexa Fluor™ 555 Conjugate	Life Technologies	C34776
Experimental models: organisms/strains		
Mouse: C57Bl/6J	The Jackson Laboratory	JAX: 000664
Mouse: Snap25-GCaMP6s (Snap25tm3.1Hze)	The Jackson Laboratory	JAX: 025111
Mouse: Slc17a6-Cre	The Jackson Laboratory	JAX: 016963
Mouse: Gad2-Cre	The Jackson Laboratory	JAX: 010802
Mouse: Slc32a1-Cre	The Jackson Laboratory	Jax: 028862
Mouse: Slc6a5-Cre	Sherman et al. 2015	N/A
Mouse: RIKEN-Slc6a5-Cre	RIKEN BRC	RBRC: 10109
Mouse: Dbx1-Cre	Bielle et al. 2005	N/A
Mouse: Foxp2-Cre	The Jackson Laboratory	JAX: 030541
Mouse: Chat-Cre	The Jackson Laboratory	JAX: 006410
Mouse: Egr2-Cre	The Jackson Laboratory	JAX: 025744
Mouse: Neurod6-Cre	Schwab et al. 2000	N/A
Mouse: Penk-Cre	The Jackson Laboratory	JAX: 025112
Mouse: Parv-Cre	The Jackson Laboratory	JAX: 017320
Mouse: Tac1-Cre	The Jackson Laboratory	JAX: 021877
Mouse: Npy-Cre	The Jackson Laboratory	JAX: 027851
Mouse: ROSA-LSL-G-TVA (Gt(ROSA)26Sortm1(CAG-RABVgp4,-TVA)Arenk)	The Jackson Laboratory	JAX: 024708
Mouse: ROSA-LSL-GCaMP6s (Ai96)	The Jackson Laboratory	JAX: 028866
Mouse: ROSA-LSL-GCaMP6f (Ai95)	The Jackson Laboratory	JAX: 028865
Mouse: ROSA-LSL-EYFP	The Jackson Laboratory	JAX: 006148
Mouse: Slc17a6-Flp0	The Jackson Laboratory	JAX: 030212
R26 LSL FSF ReaChR-mCitrine	The Jackson Laboratory	JAX: 024846
RC::FLTG	The Jackson Laboratory	JAX: 026932
Software and algorithms		
Matlab	MathWorks	
Whistles	Holy and Guo, 2005	
Custom Matlab code	Yackle Lab	DOI: 10.5281/zenodo.5765668
Other		
M.O.M.® (Mouse on Mouse) Blocking Reagent	Vector Laboratories	MKB-2213-1